International Institute for
Applied Systems Analysis
I I A S A www.iiasa.ac.at

YSSP Report
Young Scientists Summer Program

Assessing water storage variability in large exorheic river basins from global hydrological models over 1948–2016

Denise Cáceres, d.caceres@em.uni-frankfurt.de

Approved by

Supervisor: Luca Guillaumot and Yoshihide Wada
Program: Water
31.10.2020
This report represents the work completed by the author during the
IIASA Young Scientists Summer Program (YSSP) with approval from the
YSSP supervisor.

It was finished by the 31st of October 2020 and has not been altered or
revised since.

Yoshihide Wada   *L. Guillaumot*

ZVR 524808900

Table of Contents

Abstract

Total land water storage anomalies (TWSAs) give valuable insights as to the hydrological behaviour of a basin and, as such, constitute one of the basin signatures. However, to this day, an accurate assessment of this hydrological variable remains a challenge. The Gravity Recovery and Climate Experiment (GRACE) mission enabled its monitoring at global scale. However, these observations are limited in time and do not give information as to the individual components and drivers of TWSAs. This variable can also be estimated by the means of global hydrological models (GHMs). Here, we did a long-term assessment (1948–2016) of TWSAs in 17 large exorheic basins worldwide using two state-of-the-art GHMs, namely the Community Water Model (CWatM) and WaterGAP. TWSAs were decomposed into individual mass components by the means of the models, and into individual temporal signals (seasonal, linear trend and interannual) by the means of harmonic analysis. In a first instance, the models were validated against GRACE-based TWSAs aggregated over the global continental area (except Greenland and Antarctica) for the time period 2002–2016. Model evaluation was also performed against in situ streamflow observations and showed a highly variable model performance depending on the model and gauging station considered. The long-term assessment of TWSAs and individual mass and temporal components revealed the importance of seasonal and annual water storage fluctuations in the soil, groundwater and river compartments. The comparison between CWatM and WGHM showed significant model discrepancy with respect to anomalies in these water storage compartments. These discrepancies are presumably related to different model parameterization as to maximum soil water storage capacity, groundwater recharge and groundwater abstractions for human use, and to the fact that WaterGAP was calibrated against observed mean streamflow. Furthermore, we found an El Niño-Southern Oscillation (ENSO) signature in the interannual signal of TWSAs by the means of a correlation analysis against the Multivariate ENSO Index (MEI).

Acknowledgments

About the authors

Denise Cáceres is a fourth-year doctoral candidate in the Hydrology Working Group of Prof. Dr. Döll at the Institute of Physical Geography of the Frankfurt Goethe University (Germany). She currently works at the International Centre for Water Resources and Global Change (UNESCO) of the German Federal Institute of Hydrology. (Contact: d.caceres@em.uni-frankfurt.de)

1. Introduction

Water on continents in the form of liquid and ice is stored in multiple terrestrial water storage compartments, like glaciers, aquifers and surface water bodies (SWBs). The aggregation of the water mass in all of these compartments is commonly referred to as total land water storage (TWS). This amount can vary over time, depending on meteorological factors (precipitation, surface temperature etc.) and also on direct human interventions, like the impoundment of water in artificial reservoirs and the abstraction of water for sectoral use (domestic, industrial etc.). To calculate the water balance of a river basin over a specific time period, it is necessary to compute the TWS mass change, which is equal to the final TWS mass minus the initial one, and can be calculated as follows (Rodell, 2004; Di Long et al., 2014):

$$\Delta TWS = P - Q - ET \qquad (1)$$

where P is the total precipitation, Q is the net streamflow (the streamflow that leaves the basin minus the upstream streamflow that enters the basin) and ET is the evapotranspiration. However, to determine mass changes over a specific time period, it is necessary to compute mass anomalies, which are mass variations as compared to the mean value over this period.

TWS anomalies (TWSAs) constitute one of the basin signatures. They can be of interest when studying water transfers from continents to oceans (Reager et al., 2016; Rietbroek et al., 2016; Wada et al., 2017; Cazenave et al., 2018), and they can also be used to detect long-term effects of human interventions (Döll et al., 2014; Wang et al., 2018) on continental water storage, as well as cycles related to natural climate variability (Llovel et al., 2011; Humphrey et al., 2016). TWSAs can be estimated through the processing of observations collected by the satellites of the Gravity Recovery and Climate Experiment (GRACE) mission or through the application of global hydrological models (GHMs). To this day, however, an accurate assessment of this hydrological variable remains a challenge, given the interaction between multiple terrestrial storages and the superposition of multiple temporal signals (subseasonal, seasonal, interannual etc.).

Even though the sources of uncertainty are better understood in the case of GRACE-derived TWSAs, the time series available from these observations only start in 2002 and contain significant gaps due to, for example, instrument malfunction. Another limitation of GRACE-derived products is the coarse spatial resolution (~300 km). Regarding TWSAs derived from GHMs, there is still a lack of consensus on how to quantify the uncertainty due to each individual source (input climate data, model structure, parameterization, calibration etc.) and the resulting total uncertainty. A common practice in the hydrological modelling community is the usage of an ensemble of GHMs instead of a single one; the spread between the different models is then used as an informal indication of uncertainty. Despite the still poorly understood sources of uncertainty, the usage of GHMs offers many advantages over GRACE, like the possibility of reconstructing the signal before 2002, of decomposing the total signal into individual compartments (i.e. looking at the parts to understand the whole) and of detecting human influences on the signal, and a finer spatial resolution than GRACE.

TWSAs have been estimated over the global continental area (Munier et al., 2012; Dieng et al., 2015; Cáceres et al., 2020), as well as over the global exorheic (i.e. draining into the ocean) and endorheic (i.e. hydrologically landlocked) systems, and the individual endorheic regions worldwide (Wang et al., 2018). In this study, we investigated TWSAs in 17 large exorheic basins worldwide over 1948–2016 by the means of two global hydrological models, namely the Community Water Model (Burek et al., 2020), hereafter CWatM, and the WaterGAP Global Hydrology Model (Müller Schmied et al., 2020),

hereafter WGHM. The basins were chosen to represent different climates, continents, sizes and levels of human pressure. TWSAs were decomposed into individual mass components (i.e. anomalies in water storage compartments), on the one hand, and into individual temporal components, on the other hand. In this way, it was possible to identify and analyze the main natural and anthropogenic drivers of TWSAs in large exorheic basins.

Through this assessment, we aimed to address the following questions:
- How did water storage vary in large exorheic basins over 1948–2016?
- Can we detect the influence of natural climate variability and/or direct human interventions on TWSAs in large exorheic basins over this period?
- What can we learn about uncertainty in modelled TWSAs in large exorheic basins from the comparison between CWatM and WGHM?

In the following section, we describe the methods and data sets used in this study. In Sect. 3, we present the results of our assessment and discuss them. Finally, we present our conclusions in Sect. 4.

2. Methods and data

2.1. Description of the two Global Hydrological Models

2.1.1. General modelling framework

The Community Water Model (Burek et al., 2020) and the WaterGAP Global Hydrology Model (Müller Schmied et al., 2020) were used to derive monthly anomalies in TWS and individual water storage compartments, as well as monthly streamflow over a 0.5° by 0.5° grid (55 km by 55 km at equator and ~3000 km^2 grid cell) covering the global continental area except for Greenland and Antarctica. This grid was defined using the WATCH-CRU land-sea mask (this is a standard defined within ISIMIP, www.isimip.org, last access: 14 October 2020).

These two GHMs were designed with the aim of assessing past and future global and regional water availability on continents. They follow a similar modelling concept that merges conceptual and physical principles. They simulate vertical water flow and storage in soil layers, as well as exchanges with the underlying groundwater storage. Evapotranspiration (around 60 % of the water budget globally) depends on estimated potential plant demands and water availability in the soil. Rivers are fed by surface runoff occurring when precipitation exceeds soil infiltration capacity or when soils are saturated. In addition, groundwater feeds rivers with a simple conceptual approach. The stream network used to laterally route streamflow until it reaches the ocean or an inland sink is based on the global drainage direction map DDM30 (Döll and Lehner, 2002). Human interventions are included in the form of water abstractions from surface water and groundwater (Sect. 2.1.3) and the filling and regulation of artificial reservoirs (Sect. 2.1.2). Calibration is performed against streamflow observations at rain gauge stations. For this study, only WGHM was calibrated.

As input, CWatM and WGHM require daily meteorological data sets of precipitation, near-surface air temperature and other meteorological variables, depending on the model. Here, we used a homogenized climate forcing resulting from the combination of WATCH Forcing Data (WFD) based on ERA-40 reanalysis (Weedon et al., 2011) for the period 1948–1978 and WFD methodology applied to ERA-Interim reanalysis (Weedon et al., 2014) for the period 1979–2016 (Müller Schmied et al., 2016). Monthly sums of precipitation are bias corrected by a monthly precipitation data set derived from rain

gauge observations of the Global Precipitation Climatology Centre (GPCC) v5/v6 (Schneider et al., 2015). Hereafter, we refer to this meteorological forcing data set as WFDEI-GPCC. The models also require several input maps at 0.5° resolution, or finer when sub-grid variability is taken into account, like topography, land cover and soil texture.

The models can be run in anthropogenic (i.e. including human interventions) or naturalized mode (i.e. assuming no human interventions). Here, we compared the results obtained in anthropogenic mode to the ones obtained in naturalized mode in order to better identify human-driven water storage variations. TWSAs were aggregated over the global continental area (except for Greenland and Antarctica) for validation of model performance against GRACE data (Sects. 2.2 and 3.1.1), and over 17 large (> 150,000 km^2) exorheic river basins (Fig. 1) for the long-term (1948–2016) assessment of water storage variability (Sect. 3.2). According to the aridity index (AI), the Amazon, Amur, Congo, Danube Ganges, Mississippi, Orinoco, Parana, Rhine, Tocantins and Yangtze basins have a humid climate, the Yellow and Zambezi basins have a semihumid climate, and the Indus, Murray, Niger and Orange basins have a semiarid climate (Fig. 1).
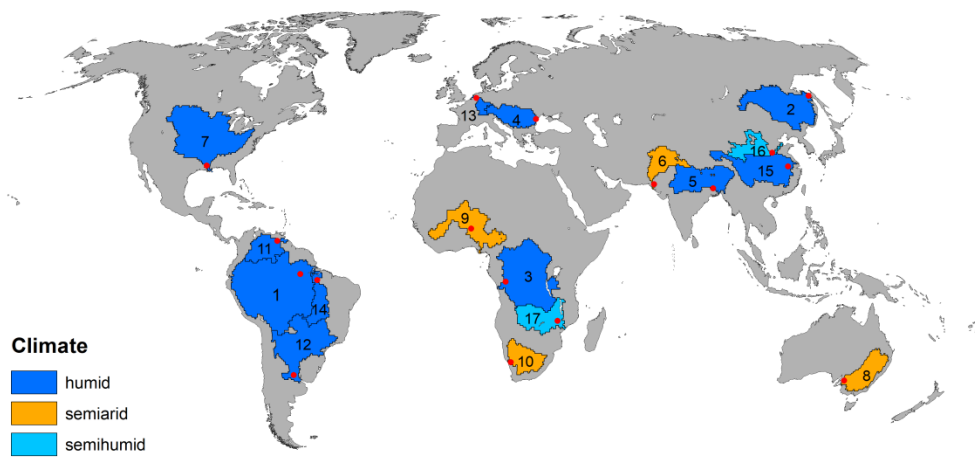
Figure 1: Distribution of exorheic river basins according to climate. The climate categories, defined according to the aridity index (AI), include semiarid (AI: 0.2–0.5, 4 basins), semihumid (AI: 0.5–0.65, 2 basins) and humid (AI > 0.65, 11 basins). The river basins include the Amazon (1), Amur (2), Congo (3), Danube (4), Ganges (5), Indus (6), Mississippi (7), Murray (8), Niger (9), Orange (10), Orinoco (11), Parana (12), Rhine (13), Tocantins (14), Yangtze (15), Yellow (16) and Zambezi (17). The in situ streamflow observation stations considered in this study for model evaluation purposes are represented by the red dots. Basin area information can be found in Table A1.

2.1.2. Individual water storage compartments

Anomalies in TWS result from the aggregation of water storage anomalies in multiple terrestrial compartments as shown in Eq. (2):

$$TWSA = GlWSA + SnWSA + CnWSA + SMWSA + GWSA + LaWSA + ReWSA + WeWSA + RiWSA \quad (2)$$

where WSA are water storage anomalies in glacier (Gl), snow (Sn), canopy (Cn), soil moisture (SM), groundwater (G), lake (La), artificial reservoir (Re) and river (Ri) compartment. Hereafter, we refer to the lake, artificial reservoir and wetland compartments as surface water bodies (SWBs). Below, we briefly describe how the water storage dynamics are represented by the models in each terrestrial compartment (Table 1).

Table 1: Comparison between CWatM and WGHM regarding the representation of water storage dynamics in individual terrestrial compartments.

Storage	CWatM	WGHM
Glacier	Not included.	
Snow	Similar representation at subgrid scale.	
Canopy	Similar representation.	
Soil	3 layers (the 2 upper layers constitute the effective root zone). Runoff generation is a function of saturation in the 2 upper layers.	One-layer linear storage (effective root zone). Runoff generation is a function of soil saturation and the runoff coefficient γ.
Groundwater	One-layer linear storage that distinguishes between a renewable (limited) and a non-renewable part (unlimited). Filled by diffuse groundwater recharge and preferential bypass flow. Drained by groundwater discharge to surface water storage, groundwater net abstractions (from renewable part) and capillary rise.	One-layer linear storage (unlimited). Filled by diffuse groundwater recharge and point groundwater recharge from SWBs[a] in (semi)arid regions. Drained by groundwater discharge to surface water storage and groundwater net abstractions.
Lake	Distinction between global (i.e. upstream area beyond the actual grid cell) and local lakes. Drained by net surface water abstractions.	Distinction between global (i.e. upstream area beyond the actual grid cell) and local lakes. Local lakes are simulated as local reservoirs. Drained by net suface water abstractions.
Wetland	Not included.	Included. No surface water abstractions.
Artificial reservoir	Representation based on simple reservoir operation algorithm. Drained by net surface water abstractions.	Representation based on simple reservoir operation algorithm. Includes local lakes as local reservoirs. Drained by net surface water abstractions.
River	Filled by inflow from upstream river and SWBs[a], (sub)surface runoff and inflow from groundwater. Drained by streamflow leaving the cell, net surface water abstractions and evaporation from river.	Filled by inflow from upstream river and SWBs[a], (sub)surface runoff and inflow from groundwater. Drained by streamflow leaving the cell and net surface water abstractions.

[a] SWBs; surface water bodies.

WGHM and CWatM include the representation of processes related to mass variations in snow but not explicitly in glaciers. To simulate snow dynamics, the models take into account the subgrid variability of elevation. Snow accumulation, melt and sublimation are modelled in separated elevation zones on subgrid level. The calculation of snow melt is based on a degree-day factor method. The canopy water storage is defined by the models as the water intercepted by terrestrial vegetation minus the part that evaporates. The interception of water, the evaporation of intercepted water and the maximum canopy storage are calculated separately per land cover class.

The representation of the soil storage differs from one model to the other. In CWatM, the soil storage consists of three separate layers, whereas in WGHM it consists of only one layer. In WGHM, the simulated water storage represents the soil moisture in the effective root zone. In CWatM, the soil moisture is redistributed within the three layers, but only the two upper layers correspond to the effective root zone. In both models, the effective root zone is defined per land cover class.

In WGHM, the total runoff generated in the grid cell depends on soil saturation and the runoff coefficient γ, which is estimated during calibration. The total runoff exits the soil compartment as an outflow and is partitioned into surface and subsurface runoff, which recharges the SWBs and the river compartment, and diffuse groundwater recharge.
In CWatM, the fraction of the grid cell that contributes to surface runoff generation is calculated as a function of the saturation in the two upper soil layers. Moreover, the model computes preferential bypass flow, i.e. the fraction of the water available for infiltration that is directly passed to the groundwater compartment by bypassing the soil layers. As surface runoff, it is calculated as a function of the saturation in the two upper soil layers; the wetter these soil layers get, the more water bypasses the soil.

The groundwater storage is represented as a one-layer linear compartment in both models. In WGHM, this storage is only computed in relative terms and is assumed to be unlimited. In CWatM, the groundwater storage is subdivided into a renewable and a non-renewable part. The renewable groundwater storage is computed in absolute terms and is included in the model's water balance equation. The deeper non-renewable groundwater storage can only be computed in relative terms and is assumed to be unlimited. In both models, the groundwater compartment is filled by diffuse groundwater recharge from the soil compartment and emptied by groundwater discharge to surface water storage and groundwater net abstractions (in CWatM, water is only abstracted from the renewable part). In WGHM, the groundwater storage is also filled by point groundwater recharge from SWBs in (semi)arid regions. In CWatM, this storage is also filled by preferential bypass flow and emptied by capillary rise.

Both models include lakes and artificial reservoirs, which are classified either as global (i.e. upstream area beyond the actual grid cell) or local (only a part of the regional river system within the actual grid cell). Lakes and reservoirs included in CWatM are based in the HydroLakes database (Lehner et al., 2011; Messager et al., 2016). Contrary to CWatM, WGHM also includes wetlands (also classified as global or local). Attributes of lakes, wetlands and reservoirs are defined in WGHM according to the Global Lakes and Wetland Database (GLWD) of Lehner and Döll (2004) and a preliminary but updated version of the Global Reservoir and Dam (GRanD) database (Döll et al., 2009; Lehner et al., 2011).

To calculate variations in the artificial reservoir water storage, the models apply a simple general reservoir operation algorithm. In WGHM, an important caveat is that local reservoirs are simulated as local lakes, and thus are included in the lake rather than the reservoir water storage compartment. This modelling choice was made because 1) the required lumping of all local reservoirs within a grid cell into one reservoir erases the specific characteristics of each individual reservoir and 2) local

reservoirs are likely not on the main river simulated in the grid cell but on a tributary. Hence, it is assumed that local reservoirs are not necessarily better simulated by the reservoir algorithm than by the lake one.

In both models, the river storage compartment is filled by streamflow from upstream cell(s), surface and subsurface runoff, inflow from upstream SWBs and groundwater (baseflow), and emptied by the streamflow that leaves the cell and net abstractions from river. In contrast to WGHM, CWatM also accounts for evaporation from river.

2.1.3.   Influence of human water demand

Human water demand is supported by abstractions from surface water and groundwater. A part of the abstracted water becomes consumptive water use (i.e. the part that evapotranspires during use), while the rest returns to the system (i.e. return flows). Such processes influence TWSAs.

In the approach adopted by WGHM, the submodel Groundwater-Surface Water Use (GWSWUSE) reads time series of water consumption and water abstraction computed by five global water use models for five water use sectors (irrigation, domestic, manufacturing, livestock, and cooling of thermal power plants), and computes time series of potential net abstraction (i.e. total abstraction minus return flow) from surface water (NA_s) and groundwater (NA_g). WGHM reads the time series of NA_s and NA_g as input. Note that this implies the assumption of instantaneous return flows. As a result of the assumption of unlimited groundwater storage, the NA_g is always satisfied. On the other hand, the satisfaction of the NA_s is subject to the water availability in the SWBs, except for wetlands (Table 1), and the river compartment. If the surface water available for abstraction cannot satisfy the daily surface water demand (i.e. NA_s) in a given cell, then (part of) the remaining water demand can be satisfied by abstracting water from a neighbouring cell.

CWatM calculates water abstraction, water consumption and return flows for the irrigation, domestic, industry and livestock sectors. Water can be abstracted from surface water (i.e. lake, reservoir and river compartments) and groundwater (i.e. renewable storage, which is considered to be the readily extractable groundwater). The allocation of surface water and groundwater to satisfy the water demand is a function of long-term average streamflow and baseflow, according to the approach described in the study of Wada et al. (2014).

In Sect. 3.2.1, we discuss the influence of human interventions on TWSAs by comparing model outputs from anthropogenic and naturalized runs.

2.2. Model evaluation

The performance of the GHMs used here was first evaluated at global scale, through the comparison against GRACE-based globally aggregated TWSA time series, and then at basin scale, through the comparison against downstream in situ streamflow observations. Here, we used an updated version of the ensemble of four GRACE spherical harmonic (SH) solutions used by Cáceres et al. (2020). These solutions were derived by processing ITSG-Grace2018 (Mayer-Gürr et al., 2018) and GRACE Release 06 (CSR, GFZ, JPL) quasi-monthly Level-2 gravity field solutions. The resulting integrated and corrected signal corresponds to the global continental (Antarctica and Greenland excluded) mass change from hydrology and glaciers (i.e. TWSA), since it is impossible for GRACE to make the distinction.

This implies that a direct comparison between modelled and GRACE-based anomalies is not possible, because the models do not explicitly compute water storage anomalies related to glacier mass change. To account for the missing glacier compartment, we summed glacier water storage anomalies obtained with the global glacier model of Marzeion et al. (2012) (hereafter GGM) to the TWSAs computed by the GHMs.

Monthly time series of streamflow observed at gauging stations were collected from the online data portal of the Global Runoff Data Centre (GRDC), 56068 Koblenz, Germany. For each basin, the most downstream station with a minimum of 6 consecutive (i.e. with no gap) years with monthly observations was selected. For more information concerning the stations, see Table A2 in the Appendix.

2.3. Temporal disaggregation and influence of natural climate variability

Aside from the disaggregation into individual water storage (or mass) components, TWSA time series can also be temporally disaggregated following Eq. (3):

$$TWSA = TWSA_{long-term} + TWSA_{annual} + TWSA_{semiannual} + TWSA_{residual} \quad (3)$$

where $TWSA_{long-term}$ is the long-term linear trend, $TWSA_{annual}$ and $TWSA_{semiannual}$ are the annual and semiannual cycles, respectively, and $TWSA_{residual}$ is the remaining part (i.e. after removal of the long-term linear trend, the annual and semiannual cycles) of the overall signal (TWSA). Here, the temporal decomposition of TWSA was done by simultaneously fitting harmonic functions (sines and cosines) to the data using standard linear least squares regression. Monthly de-seasonalized TWSA were obtained by removing the annual and semiannual cycles, monthly de-trended TWSA were obtained by removing the long-term linear trend over the full period, and monthly residual TWSA were obtained by removing all of the above. The de-seasonalized time series were used to highlight the long-term linear trend component (if present) in the overall signal. The de-trended time series were used to give prominence to the seasonal component. As to the residual (i.e. de-seasonalized and de-trended) time series, they may include interannual and subseasonal signals and noise; here, we assumed that most of the residual signal represents interannual variability. This being said, here we attempted to relate interannual TWSA fluctuations to natural climate variability.

Large-scale natural climate phenomena alter water exchanges between atmosphere, oceans and continents. The patterns associated to these phenomena are often described by the means of indicators which represent climate variations by distances around a mean value over a given period (i.e. climate indices).

The El Niño-Southern Oscillation (ENSO) is a naturally occurring anomalous state of tropical Pacific coupled ocean-atmosphere conditions. It is one of the most influential natural climate patterns on Earth. ENSO events alternate between two opposite phases, El Niño and La Niña, on an interannual timescale. El Niño and La Niña alternately warm and cool large areas of the tropical Pacific Ocean, which has a significant influence over the associated rainfall patterns. During El Niño, the primary location of moist, rising air (over the warmest water) is centered over the Central or Eastern Pacific and, during La Niña, over Indonesia and the Western Pacific.

Many studies have investigated the influence of the ENSO on land hydrology (Cazenave and Llovel, 2010; Llovel et al., 2011; Cazenave et al., 2012; Boening et al., 2012; Munier et al., 2012). Here, we investigated the relation between basin-scale TWSAs and ENSO-driven climate variability, by comparing the interannual (i.e. residual) TWSAs to Multivariate ENSO Index (MEI) version 2

intensities (Wolter and Timlin, 1993; Wolter and Timlin, 1998) over 1979–2016 (the period was chosen according to the availability of MEI data). The MEI combines both oceanic and atmospheric variables, namely sea level pressure (SLP), sea surface temperature (SST), zonal and meridional components of the surface wind, and outgoing longwave radiation (OLR) over the tropical Pacific basin (30°S–30°N and 100°E–70°W). It provides in a single index an assessment of the ENSO, with positive MEI values indicating El Niño events and negative MEI values indicating La Niña events.

3. Results and discussion

3.1. Evaluation of model performance against independent observation-based data

3.1.1. Comparison to GRACE-based global TWSAs

Figure 2a shows global monthly TWSAs computed by CWatM and WGHM, which correspond to mass changes from hydrology only (the models do not include a glacier compartment). Global monthly GlWSAs computed by GGM were added to TWSAs from the GHMs for comparison against the GRACE ensemble mean (Fig. 2b). Glaciers lead to a much stronger decreasing trend in modelled TWSAs that is much closer yet still underestimated as compared to the trend seen by GRACE over 2002–2016 (especially in the last 3 years). Glaciers also have a slight effect on the overall seasonality, reflecting the accumulation and melting seasons within a glacier mass balance year. In general, the comparison of the resulting modelled TWSAs against the GRACE ensemble mean shows a remarkable fit in terms of NSE and r. From these results, we infer that CWatM and WGHM have a good performance at global scale in terms of TWSAs, which makes us confident in using these outputs.
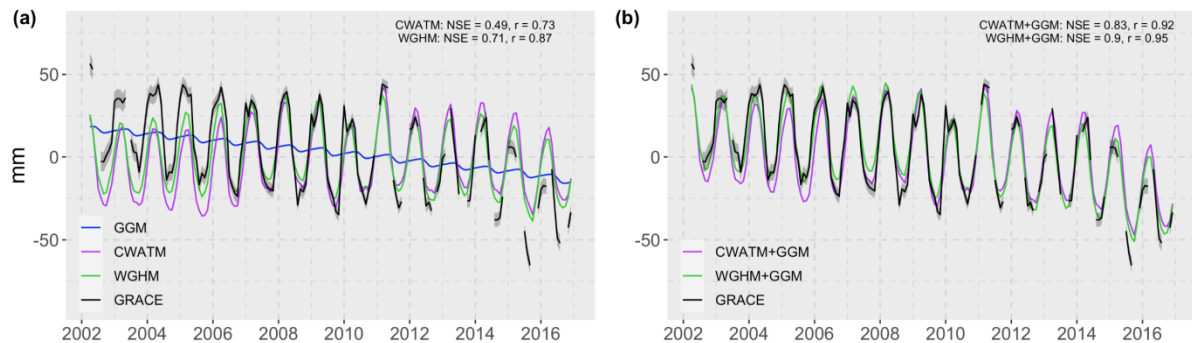

Figure 2: Global monthly TWSAs from GRACE observations and from models over April 2002 to December 2016. (a) TWSAs (hydrology and glaciers) based on GRACE ensemble (the black curve represents the ensemble mean and the shaded area around it is the uncertainty range) and computed by CWatM and WGHM (hydrology only), and GlWSAs (Eq. 2) computed by GGM. (b) TWSAs based on GRACE ensemble and modelled TWSAs (hydrology and glaciers) obtained by adding anomalies from GHMs (CWatM and WGHM) and GGM. Nash–Sutcliffe efficiency (NSE) and Pearson-correlation coefficient (r) obtained by comparing GRACE (ensemble mean) and models are provided. Anomalies are relative to the mean over January 2006 to December 2015. Millimeters represent a land water height over the global continental area without the ice sheets (132.3×10^6 km^2).

3.1.2. Comparison to in situ streamflow observations

The models show a reasonably good performance according to the Pearson correlation coefficient r (i.e. r ≥ 0.50) in 14 out of the 17 basins (Table 2). This means that, in these basins, there is a linear correlation between observed and modelled monthly streamflow. In other words, the observed and

modelled time series show a similar seasonality (Fig. 3). Note that low r values for both models in the Niger basin are attributed to the poor quality of the input data corresponding to this region.
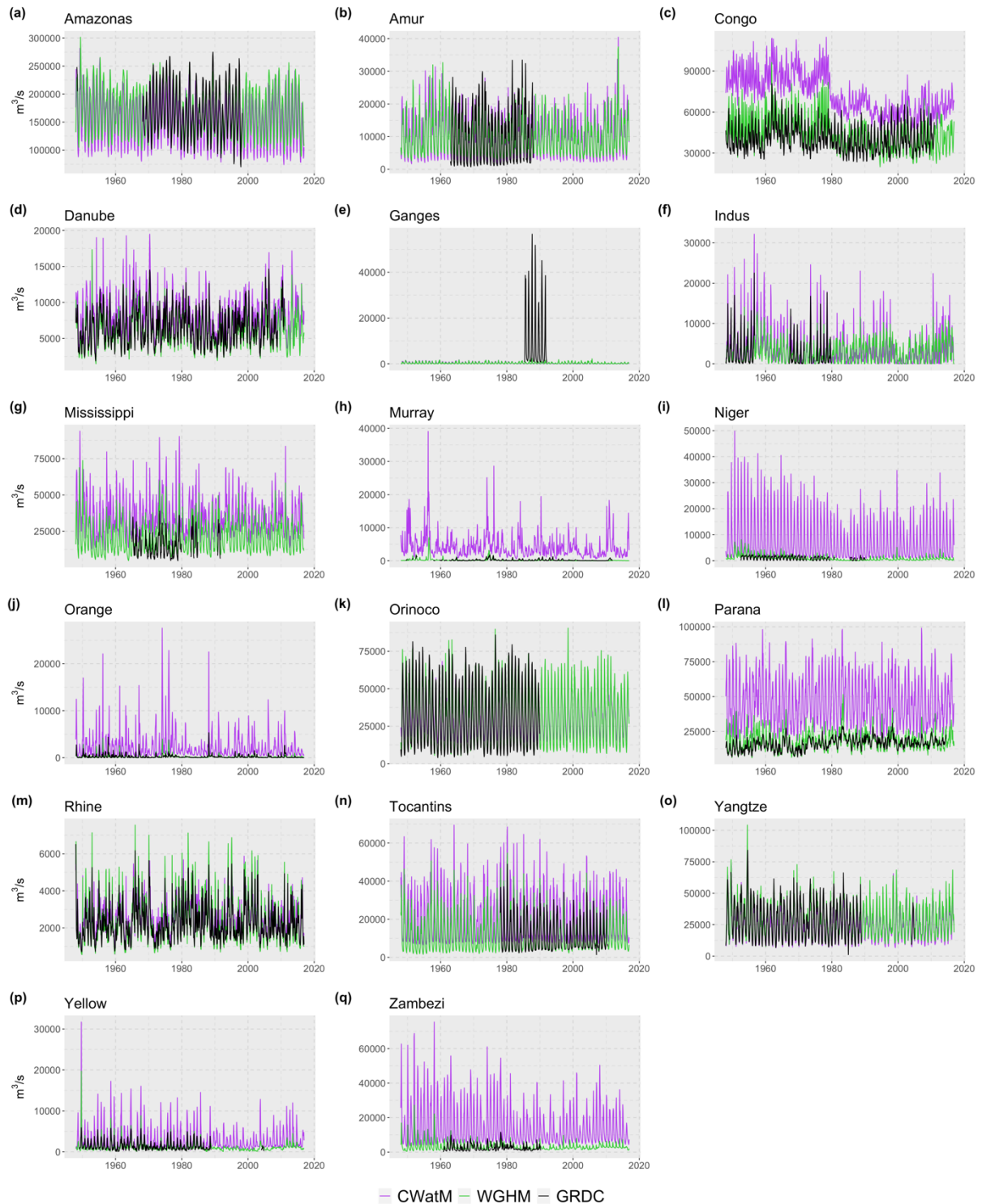

Figure 3: Comparison between observed and modelled monthly streamflow in 17 exorheic basins. Observations were collected from the online data portal of the Global Runoff Data Centre (GRDC), 56068 Koblenz, Germany. The location of the gauging stations is shown in Fig. 1. Modelled time series were obtained with CWatM and WGHM.

The results differ more from one model to the other in terms of NSE. WGHM shows a reasonably good performance (i.e. NSE ≥ 0.50) in 8 out of the 17 basins, whereas this is true for CWatM in only

4 out of the 17 basins (Table 2). This marked difference in model performance is not surprising and was even expected since WGHM was constrained to fit better to mean annual streamflow observations through its calibration procedure. Thus, it is not surprising that WGHM has higher NSE values, given that this criterion reflects in part how the model performs as compared to the mean of the observed time series. In this sense, one should note that the r values provide a fairer comparison between the two models. Furthermore, it may also be noted that, in 7 (12 in the case of WGHM) out of the 17 basins, both models show a positive NSE (Table 2), which means that they are better predictors than the observed mean.

Table 2: Goodness of fit between observed and modelled monthly streamflow in 17 exorheic basins based on the Nash-Sutcliffe Efficiency (NSE) and the Pearson correlation (r) coefficients (time series are shown in Fig. 3).

River / Station	r (CWatM)	r (WGHM)	NSE (CWatM)	NSE (WGHM)
Amazonas / Obidos-Porto	0.74	0.91	0.31	0.83
Orinoco / Puente-Angostura	0.9	0.89	0.74	0.79
Tocantins / Tucurui	0.9	0.93	-0.66	0.84
Parana / Timbues	0.53	0.75	-60.11	-0.34
Rhine / Lobith	0.92	0.94	0.54	0.67
Danube / Ceatal-Izmail	0.84	0.91	0.15	0.79
Niger / Gaya	0.28	0.38	-314.69	-1.54
Congo / Kinshasa	0.4	0.68	-12.94	-0.04
Zambezi / Matundo-Cais	0.62	0.61	-75.52	0.09
Orange / Vioolsdrif	0.66	0.62	-62.36	0.23
Mississippi / Tarbert-Landing	0.79	0.9	-8.14	-0.24
Indus / Kotri	0.85	0.85	0.14	0.7
Ganges / Hardinge-Bridge	0.72	0.7	-0.51	-0.5
Yellow / Huayuankou	0.84	0.73	-5.75	0.24
Yangtze / Datong	0.92	0.93	0.78	0.86
Amur / Bogorodskoye	0.86	0.87	0.73	0.69
Murray / Lock-1-Downstream	0.36	0.6	-276.61	0.09

From this evaluation, we conclude that one should be cautious when interpreting the model outputs at basin scale. However, we want to point out that a poor performance in terms of monthly

streamflow does not automatically imply a poor performance in terms of monthly TWSAs aggregated at the basin scale.

3.2. Assessment of TWSAs in the exorheic system over 1948–2016

Hereafter, we examine the role of anomalies in individual water storage compartments on the total signal. We also compare results from anthropogenic and naturalized runs in order to identify human influences in the total signal. Model outputs are compared to infer the main sources of uncertainty in modelled TWSAs at basin scale. Moreover, we examine the contributions from individual temporal signals in TWSAs and, more particularly, the influence of ENSO-driven climate variability on the interannual component.

3.2.1. *Contribution of individual mass components*

Given its multiple integrative composition, TWSAs reflect changes in all storage compartments of the hydrological system. One of the advantages of using GHMs is the possibility to analyze the contribution of the individual storage compartments (i.e. mass components) to TWSAs. In the sample of basins analyzed here, three storage compartments, namely the soil moisture, groundwater and river, make up a considerable part of the total signal (Fig. C1–C17 in the Appendix).

In general, the models agree on the pattern of the soil moisture anomalies. However, in all the basins (except for the Mississippi and Rhine), the amplitude of the fluctuations is significantly larger with CWatM. We suspect that this might be partly related to a difference in the definition of the maximum soil water storage capacity within the models. For instance, the study of Tangdamrongsub et al. (2018), which compared TWS change from multiple GHMs, found that WGHM showed the smallest TWS change over Australia and the North China Plain, and that this was likely related to its maximum soil water storage capacity, which was substantially lower than in the other models. Moreover, there are presumably other sources of discrepancy, like the representation of human water abstractions in the models. In the WGHM approach, direct net abstractions implicitly assume instantaneous return flows, which implies that increases in the soil water storage in irrigated areas linked to return flows are not taken into account. CWatM, on the other hand, explicitly simulates total abstractions and return flows, resulting in larger fluctuations in the soil water storage.
In addition, note that there are no significant differences between anthropogenic and naturalized runs, which is not surprising, since this compartment is not affected by human water abstractions.

Groundwater, on the other hand, is one of the major sources for water abstractions. If we consider the groundwater storage anomalies computed by WGHM, we can see that the Danube, Ganges, Indus, Mississippi and Yellow basins (Fig. C4–C7 and C16 in the Appendix) show a strongly decreasing trend in anthropogenic mode, either during the whole period (Ganges, Indus, Mississippi and Yellow) or part of it (Danube). Given that these basins contain large irrigated areas, we deduce that the groundwater depletion simulated with WGHM is due to groundwater abstractions for irrigation. This trend is likely not reproduced by CWatM because only the renewable part of the groundwater compartment is available for water abstractions. This implies that, even if the water demand has not been satisfied upon depleting the overlying hydrologically-active renewable groundwater storage, the remaining demand cannot be satisfied from the underlying nonrenewable groundwater storage.

Another noteworthy observation in relation to groundwater storage anomalies is that, in 11 out of the 17 basins (Amazon, Congo, Ganges, Mississippi, Murray, Niger, Orange, Orinoco, Parana, Tocantins and Zambezi), CWatM computes larger seasonal and/or annual fluctuations than WGHM. This might

reflect larger inflows to the groundwater compartment in the case of CWatM, in the form of diffuse recharge from the soil and/or of preferential bypass flow, which increases as a function of the saturation in the upper two soil layers. Considering that most of the basins studied here have a (semi)humid climate (Fig. 1), it is fair to assume that the upper two soil layers often reach saturation.

Regarding the river compartment, which also constitutes one of the major contributors to TWSAs, many of the basins show significant model discrepancy in the amplitude of the anomalies. We assume that this is, to a large extent, due to the fact that WGHM was calibrated (WGHM) whereas CWatM remained uncalibrated (Fig. 3).

Significant differences can also be observed in the lake storage compartment. In the Amazon, Amur, Murray and Orange basins (Fig. C1, C2, C8 and C10 in the Appendix), the anomalies computed with CWatM are of a much larger order of magnitude than with WaterGAP. However, in all of these basins, WGHM computes wetland storage anomalies of a similar amplitude and pattern than the ones in the lake compartment of CWatM. As mentioned before, CWatM does not include a wetland compartment. However, we can presume that part of the surface water storage included in WGHM as wetland water storage might be included in CWatM as lake water storage.

Nevertheless, this presumption might be wrong for some of the basins, especially in tropical regions. For instance, in the Orinoco, Parana and Tocantins basins (Fig. C11, C12 and C14 in the Appendix), WGHM computes anomalies in the wetland compartment that largely exceed the anomalies computed by CWatM in the lake compartment. In these tropical basins, it seems clear that WGHM has a larger surface water storage capacity through the inclusion of wetlands.
In addition, it is noteworthy that, in 10 out of the 17 basins (Amazon, Amur, Ganges, Mississippi, Murray, Niger, Orange, Orinoco, Parana and Tocantins), WGHM computes a larger variability in the wetland compartment than in the lake one; this shows the importance of the wetland compartment in the simulation of surface water storage variations in large exorheic basins by WGHM.

Regarding the artificial reservoir compartment, part of the model discrepancy can be attributed to how WGHM deals with local reservoirs. In the Rhine basin (Fig. C13 in the Appendix), for example, CWatM simulates anomalies in the reservoir compartment, whereas, according to WGHM, the water storage in this compartment is null. This does not necessarily mean that the reservoirs existing in this basin are neglected by WGHM, but most likely that these reservoirs are, given their characteristics, classified as local reservoirs in the model and thus simulated as local lakes. The Ganges basin (Fig. C5 in the Appendix), which exhibits significant model discrepancy in the reservoir compartment, and a larger variability in the lake compartment of WGHM than that of CWatM, may also reflect this.

Moreover, differences in the reservoir compartment also stem from the groundwater recharge scheme adopted by WGHM, which assumes that, in (semi)arid regions, besides diffuse groundwater recharge from the soil compartment, groundwater is also recharged by lakes, reservoirs and wetlands. For instance, part of the differences in reservoir storage anomalies in the Indus, Murray and Niger basins (Fig. C6, C8 and C9 in the Appendix), where groundwater recharge from SWBs occurs according to WGHM (Fig. 11d in Müller Schmied et al., 2020), can probably be explained in this way. In particular, note for the Indus basin the very negative wetland storage anomalies computed by WGHM in anthropogenic mode, which most likely indicate a recharge flow from this compartment to a depleting groundwater compartment.

Regarding the snow compartment, the models generally agree in the pattern and amplitude of the anomalies in all the basins with a significant snow mass component (Amur, Danube, Ganges, Indus, Mississippi, Rhine, Yangtze and Yellow).

3.2.2.   Contribution of individual temporal components

In 12 out of the 17 basins, namely the Amazon, Danube, Ganges, Mississippi, Niger, Orinoco, Parana, Rhine, Tocantins, Yangtze, Yellow and Zambezi, the seasonal signal in the TWSAs is the dominant temporal component (Fig. 4 and Fig. B1–B3 in the Appendix). The prominent role of the seasonality is not surprising, considering that these basins are characterized by a (semi)humid climate, except for the Niger basin (Fig. 1). Furthermore, in most of these 12 basins (all except for the Orinoco and Tocantins), the models differ significantly with respect to the amplitude of seasonal fluctuations; CWatM computes larger seasonal amplitudes in the Ganges, Niger, Parana, Yangtze, Yellow and Zambezi basins, whereas the opposite is observed in the Amazon, Danube, Mississippi and Rhine basins. As discussed in the previous subsection, model discrepancies in TWSA seasonal fluctuations stem from multiple water storage compartments (soil, groundwater, river etc.).

Unlike the Niger basin, the rest of the basins with a semiarid climate, namely the Indus, Murray and Orange (Fig. 1), show a less pronounced seasonality and, in contrast, a more pronounced interannual variability (Fig. 4 and Fig. B2–B3 in the Appendix). This is expected, given the lesser role of seasonal precipitation in this type of climate.

Interestingly, none of the basins (except for the Tocantins, Yangtze and Yellow) show a consistently decreasing or increasing trend in TWSAs over 1948–2016 (Fig. 4 and Fig. B1–B3 in the Appendix). Trends can be identified over shorter time slices. For example, the models compute an increasing trend in the Amazon over 1970–1975 (Fig. B1b), in the Orinoco over 1975–2000 (Fig. B1h) and in the Zambezi over 1950–1965 (Fig. B2q). On the other hand, some of the basins show significant model discrepancy regarding the presence or direction of these shorter linear trends. For instance, WGHM computes a distinctly decreasing trend in the Mississippi over 1975–2016 (Fig. B1e) and in the Ganges over 1990–2016 (Fig. B3e), which is not the case with CWatM; as seen in the previous subsection, this is due to differences as to how the models deal with groundwater abstractions and the satisfaction of water demand. Conversely, CWatM computes a distinctly decreasing trend in the Congo over 1980–2000 (Fig. B2b) that is not reproduced by WGHM.
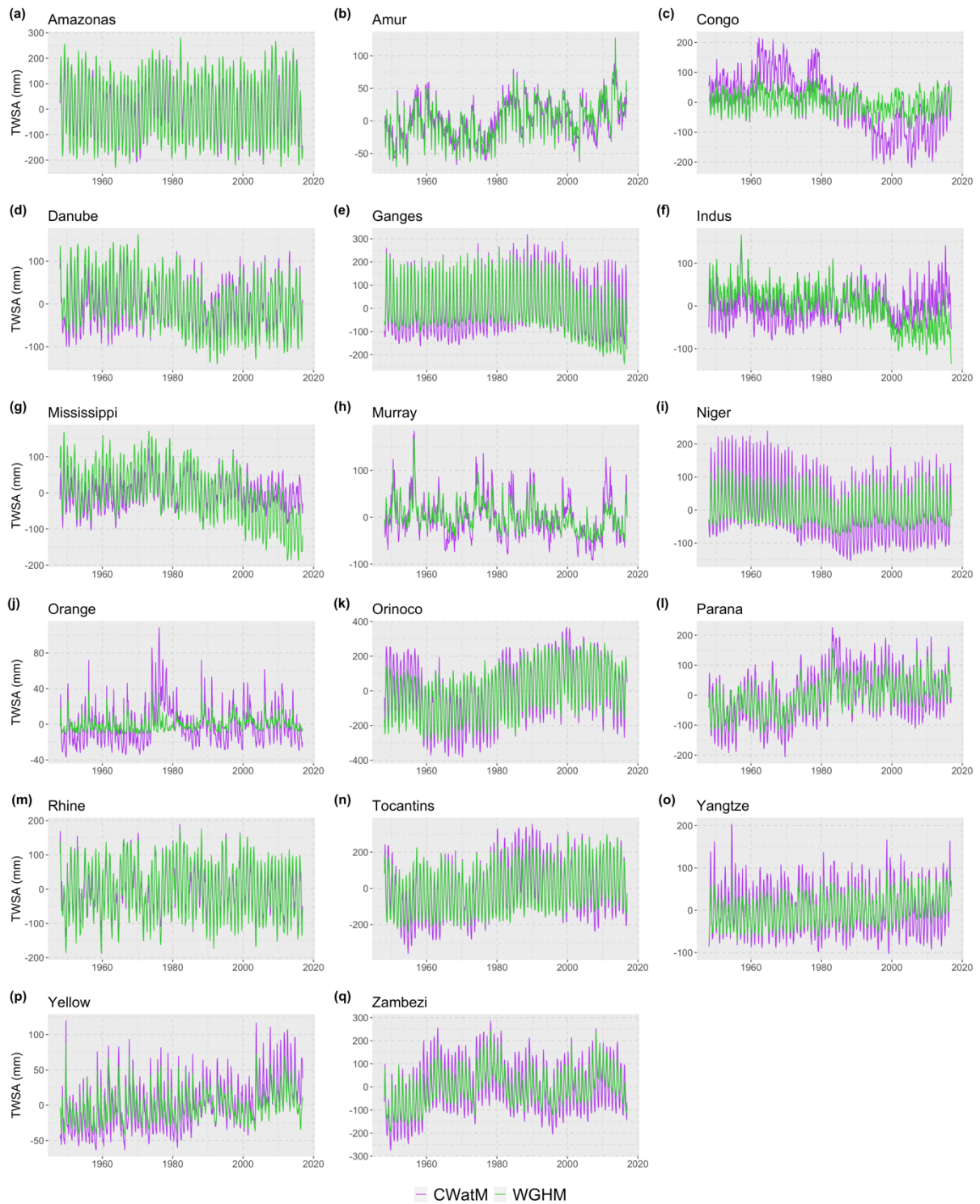
Figure 4: Comparison between monthly TWSAs from CwatM and WGHM in 17 exorheic basins over 1948–2016. Anomalies are relative to the mean over January 1948 to December 2016. Millimeters represent a land water height over the basin area.

3.2.3. Correlation to ENSO-driven climate variability

The comparison between interannual (i.e. residual) TWSAs and monthly MEI intensities showed non-negligeable r values for most of the basins analyzed here. The correlations found were either negative or positive, depending on how ENSO events (El Niño and La Niña) influence rainfall patterns

on land (Fig. D1 and D2 in the Appendix). The highest negative correlations were found for the Amazon basin and, in second place, for the Murray basin (Table 3 and Fig. 5 and 7). As to the highest positive correlation, it was found for the Parana basin (Table 3 and Fig. 6).

For all the South American basins, except for the Orinoco, a higher (positive or negative) correlation to MEI was achieved by time-shifting the TWSA time series three months behind the MEI time series. This shows that there is a time lag of one season between the occurrence of ENSO events over the Pacific Ocean and their impact on land water storage fluctuations over a large part of South America. In the case of the Murray basin, on the other hand, time-shifting the TWSA time series worsens the correlation. This is not surprising given the proximity of this basin to the regions of the Pacific Ocean affected by ENSO events.
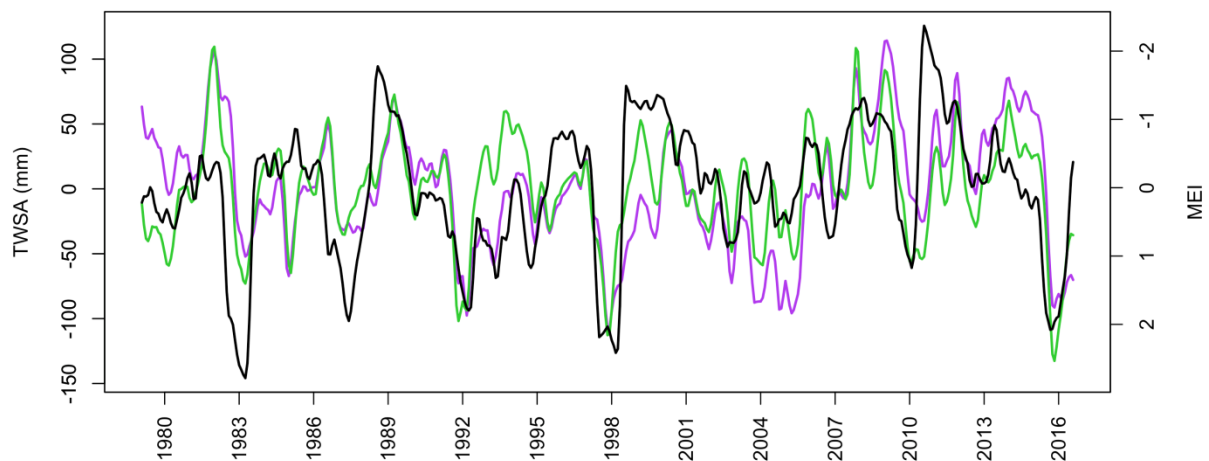

Figure 5: Correlation between de-seasonalized and de-trended monthly TWSAs and MEI intensities in the Amazon basin over 1979–2016. Intensities in Multivariate ENSO index (MEI) version 2 (black curve) were collected from official website of the NOAA Physical Sciences Laboratory. TWSAs were computed by CWatM (magenta curve) and WGHM (green curve) and shifted one season (i.e. 3 months) behind the MEI time series. All of the time series were smoothed based on a 3-month rolling average. Note the reversed right vertical axis.

In the Amazon basin (Fig. 5), El Niño has a dry impact whereas La Niña has a wet impact during December-February, which coincides with the summer rainy season (Fig. D1 and D2 in the Appendix). The dryer conditions prompted by El Niño (i.e. positive MEI values) result in deficit rainfall, which translates into decreasing water storage on land (i.e. negative TWSAs). Moreover, the wetter conditions prompted by La Niña (i.e. negative MEI values) result in excess rainfall, which translates into increasing water storage on land (i.e. positive TWSAs). This explains the negative correlation.

In the Parana basin (Fig. 6), El Niño has a wet impact during December-February, which corresponds to the summer rainy season (Fig. D1 in the Appendix). Unlike what is observed in the Amazon basin, El Niño (i.e. positive MEI values) causes excess rainfall, increasing in this way water storage on land (i.e. positive TWSAs), hence resulting in a positive correlation.
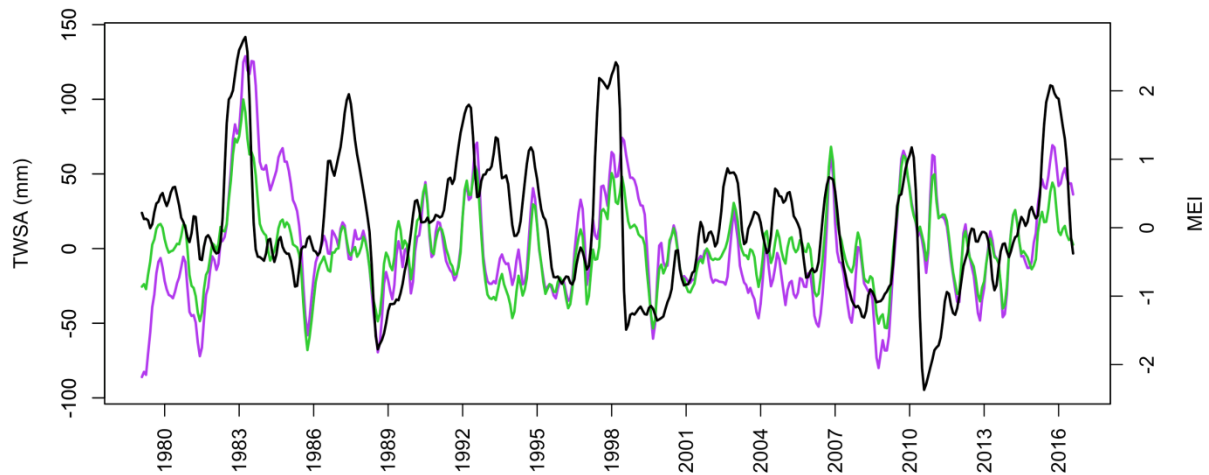
Figure 6: Correlation between de-seasonalized and de-trended monthly TWSAs and MEI intensities in the Parana basin over 1979–2016. Intensities in Multivariate ENSO index (MEI) version 2 (black curve) were collected from official website of the NOAA Physical Sciences Laboratory. TWSAs were computed by CWatM (magenta curve) and WGHM (green curve) and shifted one season (i.e. 3 months) behind the MEI time series. All of the time series were smoothed based on a 3-month rolling average.

The Murray basin is located very close to the primary location of moist, rising air during La Niña (Indonesia and Western Pacific). Thus, we can assume that this basin is quite sensitive to wetter conditions prompted by La Niña. In particular, note that the La Niña event of 2010–2011 resulted in considerably increased TWS (Fig. 7), which confirms the findings of Boening et al. (2012).

Furthermore, the results shown in Table 3 also show that the rest of the tropical basins (except for the Congo), namely the Orinoco, Tocantins and Zambezi, also exhibit a significant correlation to the MEI. This seems to confirm the findings of Llovel et al. (2011), who postulated that large tropical basins play an important role in terms of water exchange between ocean and land following ENSO events.
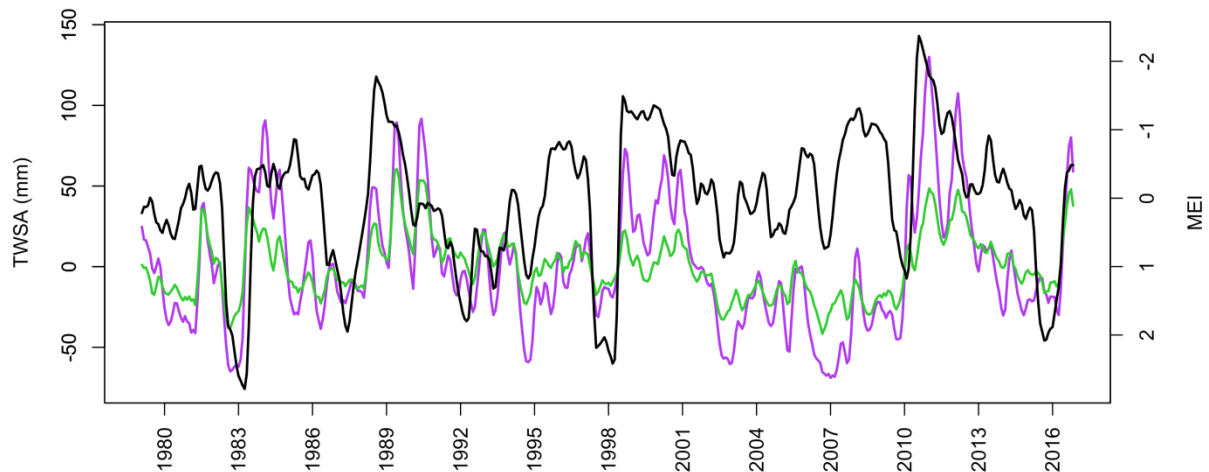

Figure 7: Correlation between de-seasonalized and de-trended monthly TWSAs and MEI intensities in the Murray basin over 1979–2016. Intensities in Multivariate ENSO index (MEI) version 2 (black curve) were collected from official website of the NOAA Physical Sciences Laboratory. TWSAs were computed by CWatM (magenta curve) and WGHM (green curve). All of the time series were smoothed based on a 3-month rolling average. Note the reversed right vertical axis.

Table 3: Pearson correlation between de-seasonalized and de-trended monthly TWSAs and MEI intensities in 17 exorheic basins over 1979–2016. All the time series were smoothed based on a 3-month rolling average. For columns 4 and 5, TWSA time series were time-shifted 3 months behind the MEI time series.

Basin	r (CWatM)	r (WGHM)	r (CwatM, 3-month time-shift)	r (WGHM, 3-month time-shift)
Amazonas	-0.19	-0.33	**-0.43**	**-0.52**
Amur	0.01	-0.01	0.1	0.07
Congo	0.1	-0.1	0.1	-0.08
Danube	-0.17	-0.15	-0.12	-0.12
Ganges	-0.24	-0.22	-0.13	-0.15
Indus	0.26	0.25	0.29	0.27
Mississippi	0.15	0.1	0.17	0.1
Murray	**-0.45**	**-0.33**	-0.32	-0.2
Niger	-0.19	-0.35	-0.18	-0.35
Orange	-0.28	-0.2	-0.37	-0.27
Orinoco	-0.3	-0.25	-0.29	-0.22
Parana	0.26	0.31	**0.41**	**0.46**
Rhine	-0.08	-0.06	-0.01	0.02
Tocantins	-0.06	-0.32	-0.24	-0.48
Yangtze	0.08	0.09	0.27	0.25
Yellow	-0.23	-0.3	-0.1	-0.26
Zambezi	-0.23	-0.29	-0.31	-0.37

3.3. Limitations and future outlook

One of the limitations with respect to the data sets used in this study relies on the fact that one of the models, in this case WGHM, was calibrated whereas the other one, namely CWatM, used a standard parameter set. As a result of this, the method employed to evaluate model performance at basin scale, which consisted in comparing model results to streamflow observations at a downstream gauging station, clearly favoured the calibrated model over the uncalibrated one.

On the other hand, we would like to point out that this does not prevent the assessment of the main sources of uncertainties (individual components and parameters) in modelled TWSAs. The difference between calibrated and uncalibrated model results also represents part of the model uncertainty, that is the part that is linked to its calibration procedure (Müller Schmied et al., 2016). It is also important

to note that, even after calibration, the contribution of each component is still uncertain due to equifinality of calibration parameters.

Another limitation is that the ensemble used in this study to represent the uncertainty in modelled TWSAs is constituted of only two GHMs.

In spite of these constraints, the preliminary analysis presented in this report, which gave major insights as to TWSAs in the exorheic system, will serve as the basis for future analysis. In the coming months, we plan to carry out a more in-depth analysis of some of the basins presented here, in order to better understand the major natural and human drivers of TWSAs and test the uncertainty related to model parameters. For this purpose, CWatM will be calibrated over the selected basins and model performance will also be evaluated against GRACE products aggregated at basin scale. Furthermore, we will look at the influence of other climate phenomena than the ENSO on TWSAs by using other climate indices, namely the Atlantic Multidecadal Oscillation (AMO), the North Atlantic Oscillation (NAO) and the Pacific Decadal Oscillation (PDO).

4. Conclusions

In this study, we assessed TWSAs in 17 large exorheic basins worldwide over 1948–2016 by applying two state-of-the-art GHMs, namely CWatM and WGHM. The majority of the selected basins are located in regions characterized by a (semi)humid climate, while the rest has a semiarid climate. In order to identify the main natural and human drivers of TWSAs, we decomposed the signal into individual mass components, corresponding to individual terrestrial water storage compartments, and into individual temporal signals. Main sources of uncertainty in modelled TWSAs were inferred by comparing the outputs from the two models.

In a first instance, we validated the models against GRACE-derived TWSAs aggregated over the global continental area (except Greenland and Antarctica). Furthermore, model performance was evaluated against in situ streamflow observations at stations located in the basins of interest; the results showed a reasonably good to poor performance depending on the station and the model considered.

The mass decomposition revealed that anomalies in the soil moisture, groundwater and river compartments make up a considerable part of the total signal in all of the basins. The temporal disaggregation showed that the seasonal signal is the dominant temporal signal in the majority of the basins. However, we also found that the basins characterized by a semiarid climate generally show a less pronounced seasonality and a more prominent interannual variability. In general, no significant decreasing or increasing trends were found in the basins of interest over 1948–2016, which means that their water storage remained more or less constant over this period. On the other hand, we detected trends over shorter time periods. In the case of WGHM, some of these trends were found to represent groundwater depletion as a result of groundwater abstractions for irrigation. Such decreasing trends were not reproduced by CWatM, given that groundwater abstractions were constrained to the part of the groundwater storage considered as renewable.

The models were found to often disagree with respect to the amplitude of seasonal and annual fluctuations. The sources of these model discrepancies are complex and linked to multiple mass components. Differences in SMWSAs seem to indicate that the models are differently constrained as to the maximum soil water storage capacity. Moreover, differences in RiWSAs are partly attributed to the fact that one of the models, namely WGHM, was calibrated against observed mean streamflow. As to GWSAs, differences are presumed to partly stem from different model parameterization in

relation to groundwater recharge. Differences in anomalies related to SWB compartments are partly linked to modelling choices as to the representation of small reservoirs and to the inclusion or absence of wetlands.

Furthermore, the comparison between TWSAs and MEI intensities revealed and ENSO signature at interannual timescale. Among the basins studied here, the Amazon, Murray and Parana were found to be particularly sensitive to ENSO-driven climate variability.

This study gives important insights as to the hydrological behaviour of large basins in the exorheic system, which can be of interest for regional sea-level change studies, given the direct water exchange between this type of basin and oceans.

Appendix A: Attributes of individual basins and streamflow observation stations

Table A 1: Basin attributes.

Basin	Latitude	Longitude	Area (km²)	Continent	Climate
Amazon	0.25	-50.25	5,921,960	South-America	Humid
Amur	53.25	140.75	1,873,890	Asia	Humid
Congo	-6.25	12.25	3,692,750	Africa	Humid
Danube	45.25	29.75	795,960	Europe	Humid
Ganges	22.75	90.75	1,570,830	Asia	Humid
Indus	23.75	67.75	836,383	Asia	Semiarid
Mississippi	29.25	-89.25	3,232,180	North-America	Humid
Murray	-35.75	139.25	1,056,750	Australia	Semiarid
Niger	4.25	6.25	1,789,490	Africa	Semiarid
Orange	-28.75	16.25	952,406	Africa	Semiarid
Orinoco	8.75	-60.75	959,504	South-America	Humid
Parana	-34.25	-58.25	2,567,720	South-America	Humid
Rhine	52.25	4.25	168,035	Europe	Humid
Tocantins	-1.25	-48.75	876,323	South-America	Humid
Yangtze	31.75	120.75	1,921,670	Asia	Humid
Yellow	37.75	118.75	757,868	Asia	Semihumid
Zambezi	-18.75	36.25	1,381,740	Africa	Semihumid

Table A 2: Attributes of streamflow observation stations from the Global Runoff Data Center (GRDC) used in this study.

River / Station	GRDC number	Latitude	Longitude	Observation period	Months with obs.
Amazonas / Obidos-Porto	3629000	-1.95	-55.51	05.1948 – 04.1998	363
Orinoco / Puente-Angostura	3206720	8.15	-63.6	01.1948 – 12.1989	504
Tocantins / Tucurui	3649950	-3.76	-49.65	01.1978 – 07.2010	372
Parana / Timbues	3265601	-32.67	-60.71	01.1948 – 08.2014	798
Rhine / Lobith	6435060	51.84	6.11	01.1948 – 12.2016	828
Danube / Ceatal-Izmail	6742900	45.22	28.72	01.1948 – 12.2010	744
Niger / Gaya	1234250	11.88	3.4	07.1952 – 09.1990	369
Congo / Kinshasa	1147010	-4.3	15.3	01.1948 – 12.2010	756
Zambezi / Matundo-Cais	1891500	-16.15	33.59	10.1960 – 04.1990	354
Orange / Vioolsdrif	1159100	-28.76	17.72	01.1948 – 12.2016	826
Mississippi / Tarbert-Landing	4127930	31.01	-91.62	01.1965 – 09.1991	204
Indus / Kotri	2335950	25.37	68.37	01.1948 – 12.1979	231
Ganges / Hardinge-Bridge	2646200	24.08	89.03	04.1985 – 03.1992	83
Yellow / Huayuankou	2180800	34.92	113.65	01.1949 – 12.2004	492
Yangtze / Datong	2181900	30.77	117.62	01.1948 – 12.2004	500
Amur / Bogorodskoye	2906901	52.53	140.47	01.1963 – 12.1987	298
Murray / Lock-1-Downstream	5404271	-34.35	139.62	07.1949 – 12.2011	639

Appendix B: Temporal disaggregation of TWSA time series
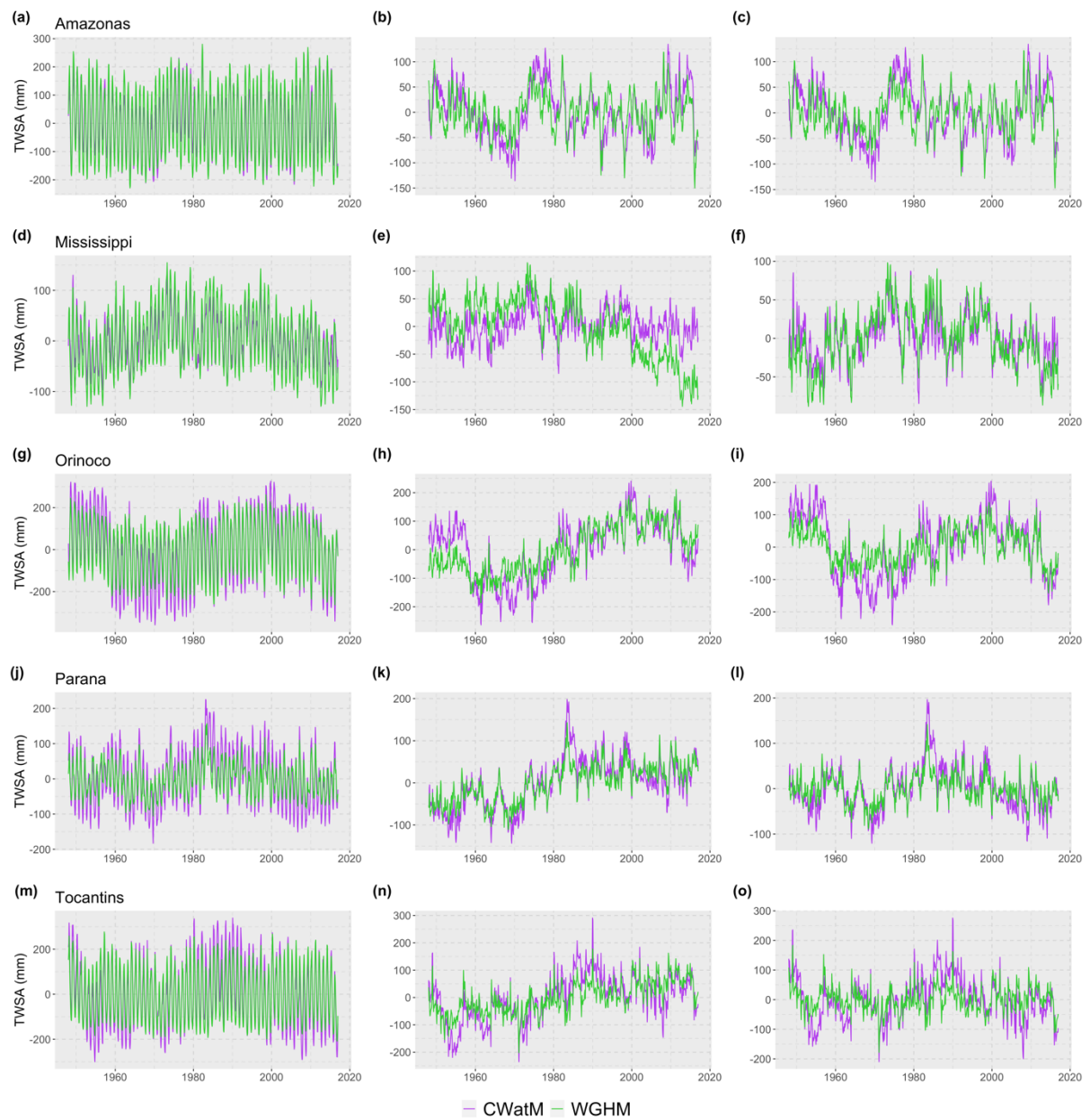
Figure B 1: Temporal disaggregation of monthly TWSA time series in large exorheic basins located in North- and South-America over 1948–2016 into (a) de-trended anomalies, (b) de-seasonalized anomalies and (c) residual (i.e. de-trended and de-seasonalized) anomalies. Anomalies were obtained by running CWatM and WaterGAP in anthropogenic mode.
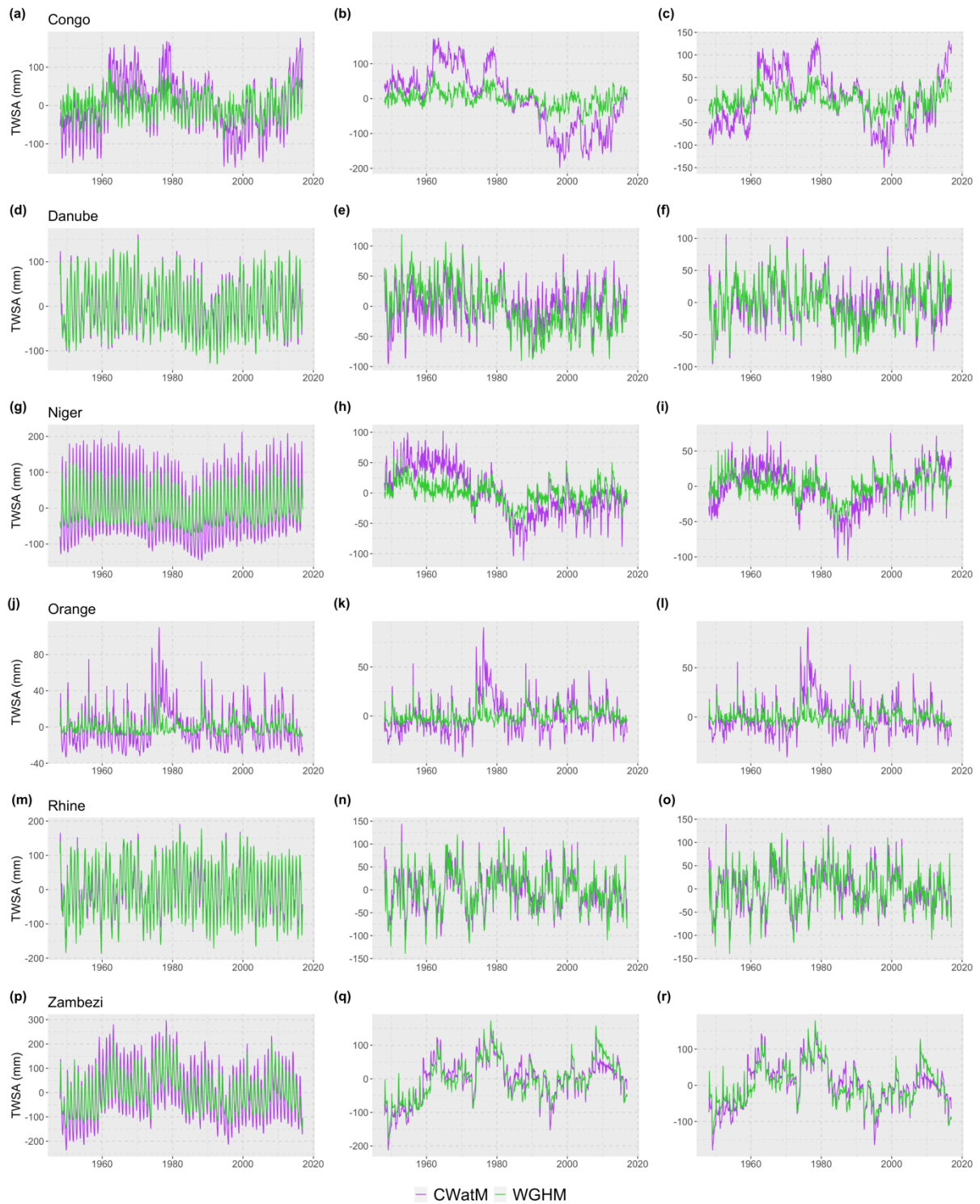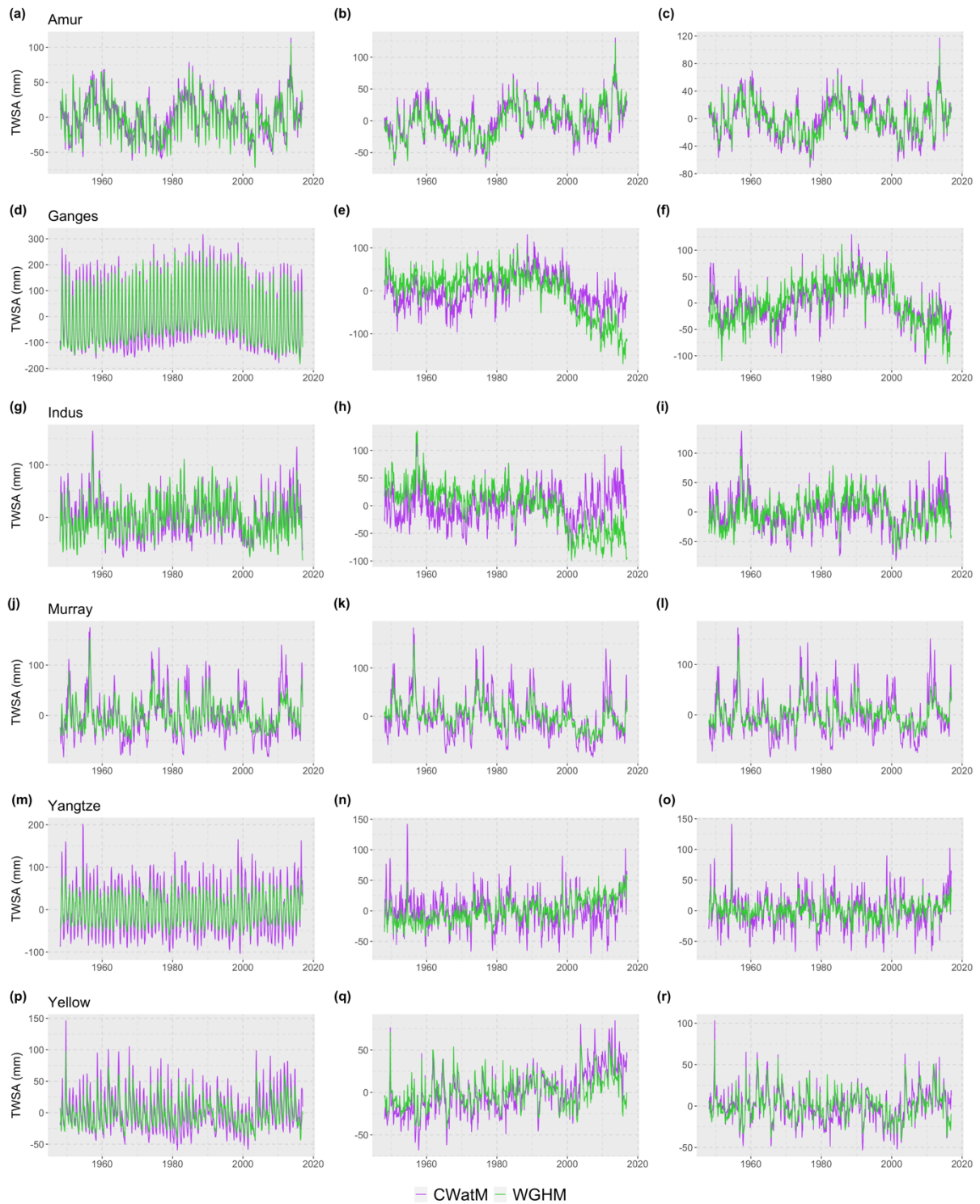
Figure B 2: Temporal disaggregation of monthly TWSA time series in large exorheic basins located in Europe and Africa over 1948–2016 into (a) de-trended anomalies, (b) de-seasonalized anomalies and (c) residual (i.e. de-trended and de-seasonalized) anomalies. Anomalies were obtained by running CWatM and WaterGAP in anthropogenic mode.

Figure B 3: Temporal disaggregation of monthly TWSA time series in large exorheic basins located in Asia and Australia over 1948–2016 into (a) de-trended anomalies, (b) de-seasonalized anomalies and (c) residual (i.e. de-trended and de-seasonalized) anomalies. Anomalies were obtained by running CWatM and WaterGAP in anthropogenic mode.

Appendix C: Mass disaggregation of TWSA time series with and without human intervention

Amazonas basin
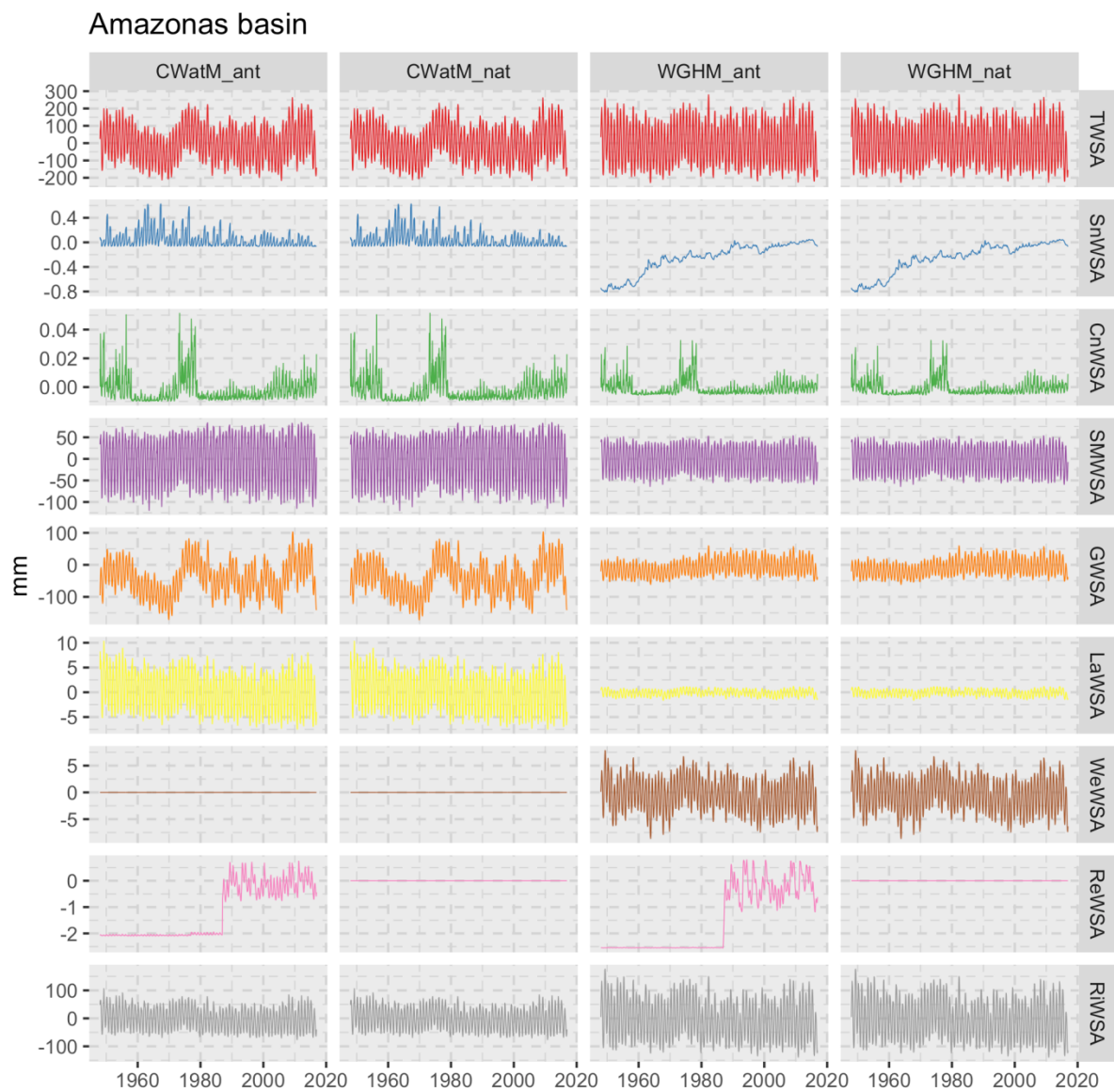
Figure C 1: Monthly TWSA and anomalies in individual water storage compartments in the Amazon basin over 1948–2016 obtained by running two global hydrological models, namely CWatM and WaterGAP, in anthropogenic (ant) and naturalized (nat) mode. Anomalies are relative to the mean over January 1948 to December 2016 and are given in millimetres of land water height over the basin area. See Equation 1 for abbreviations.
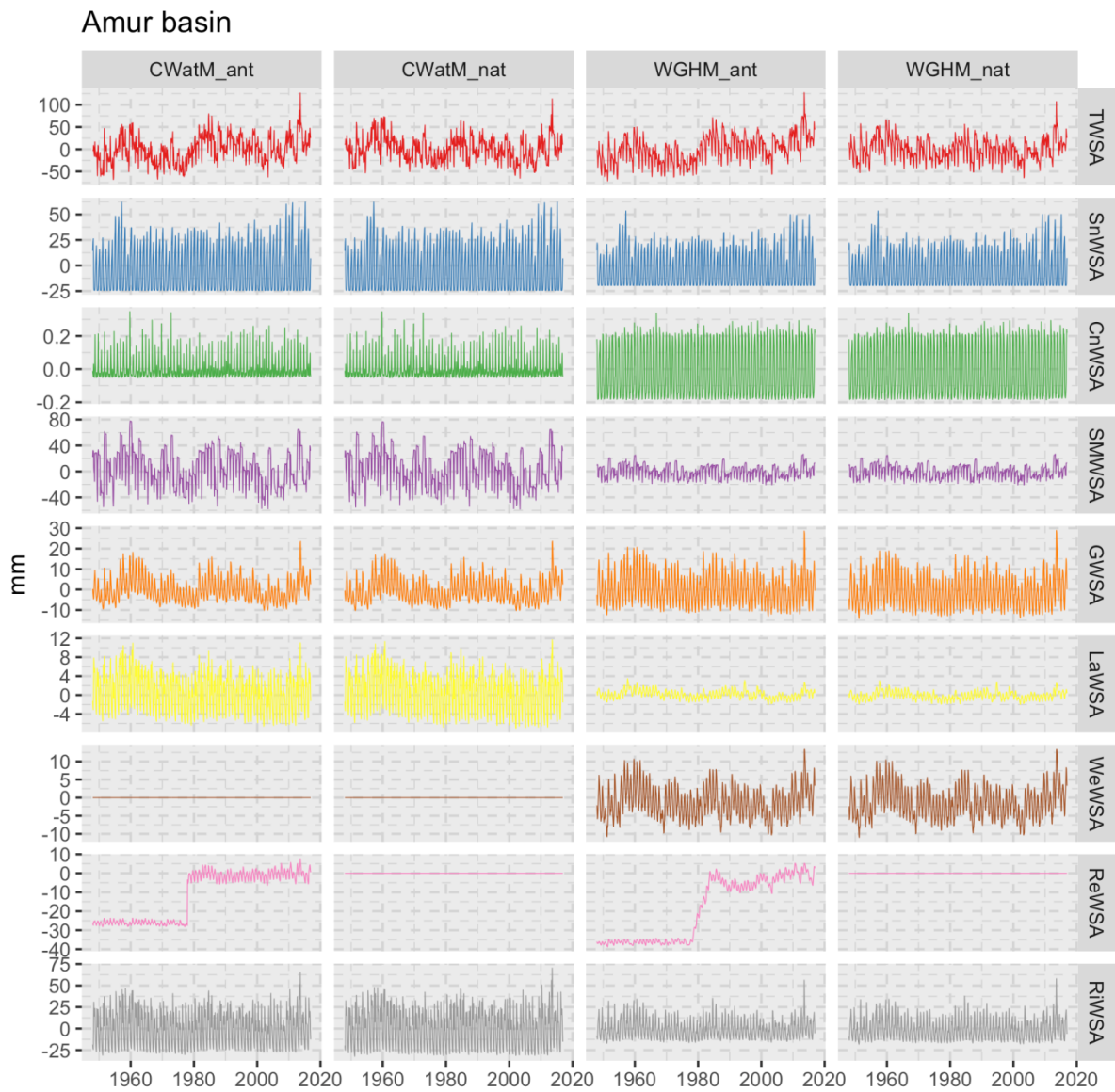
Figure C 2: As Fig. C1 but for Amur basin.
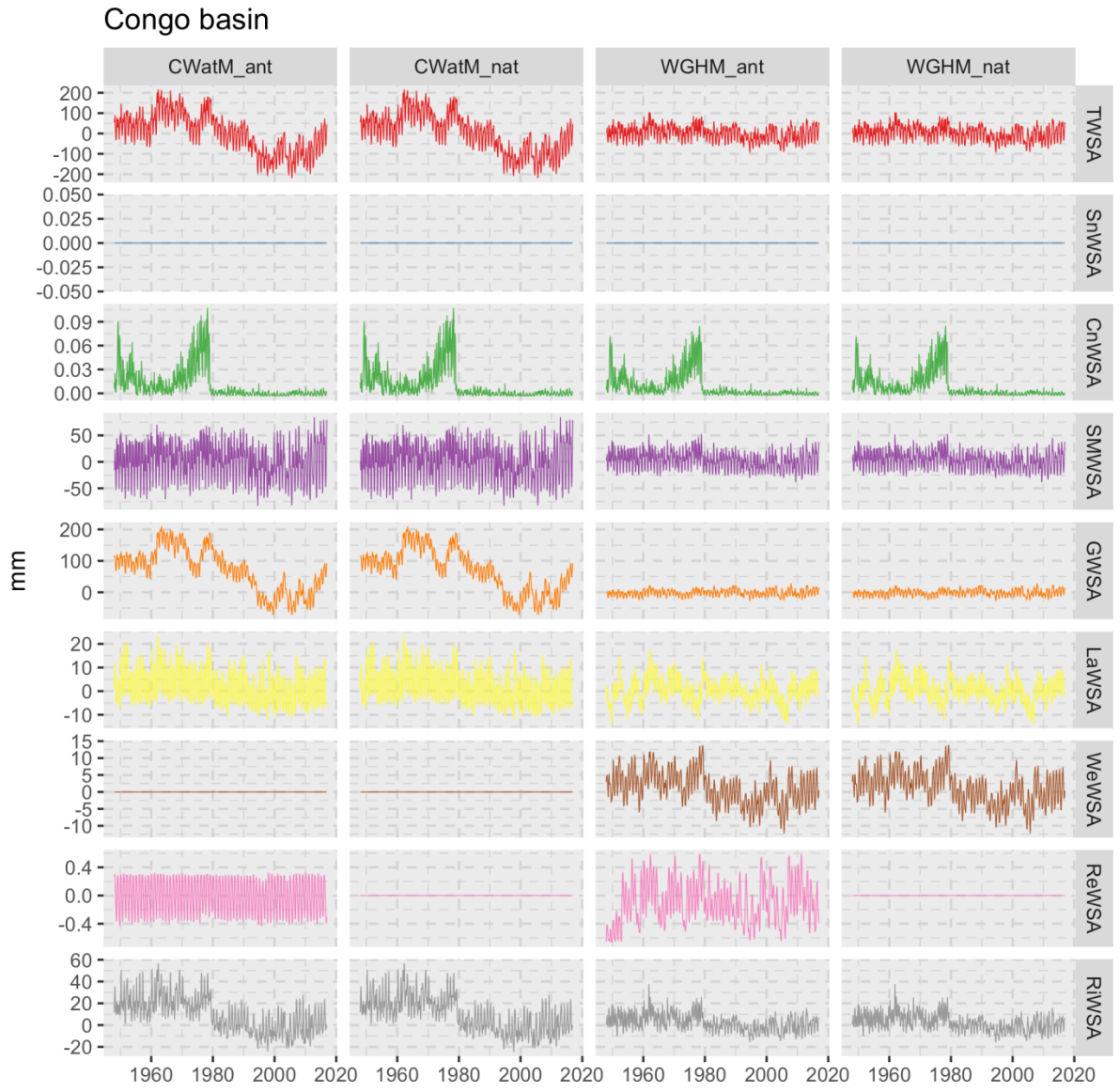
Figure C 3: As Fig. C1 but for Congo basin.
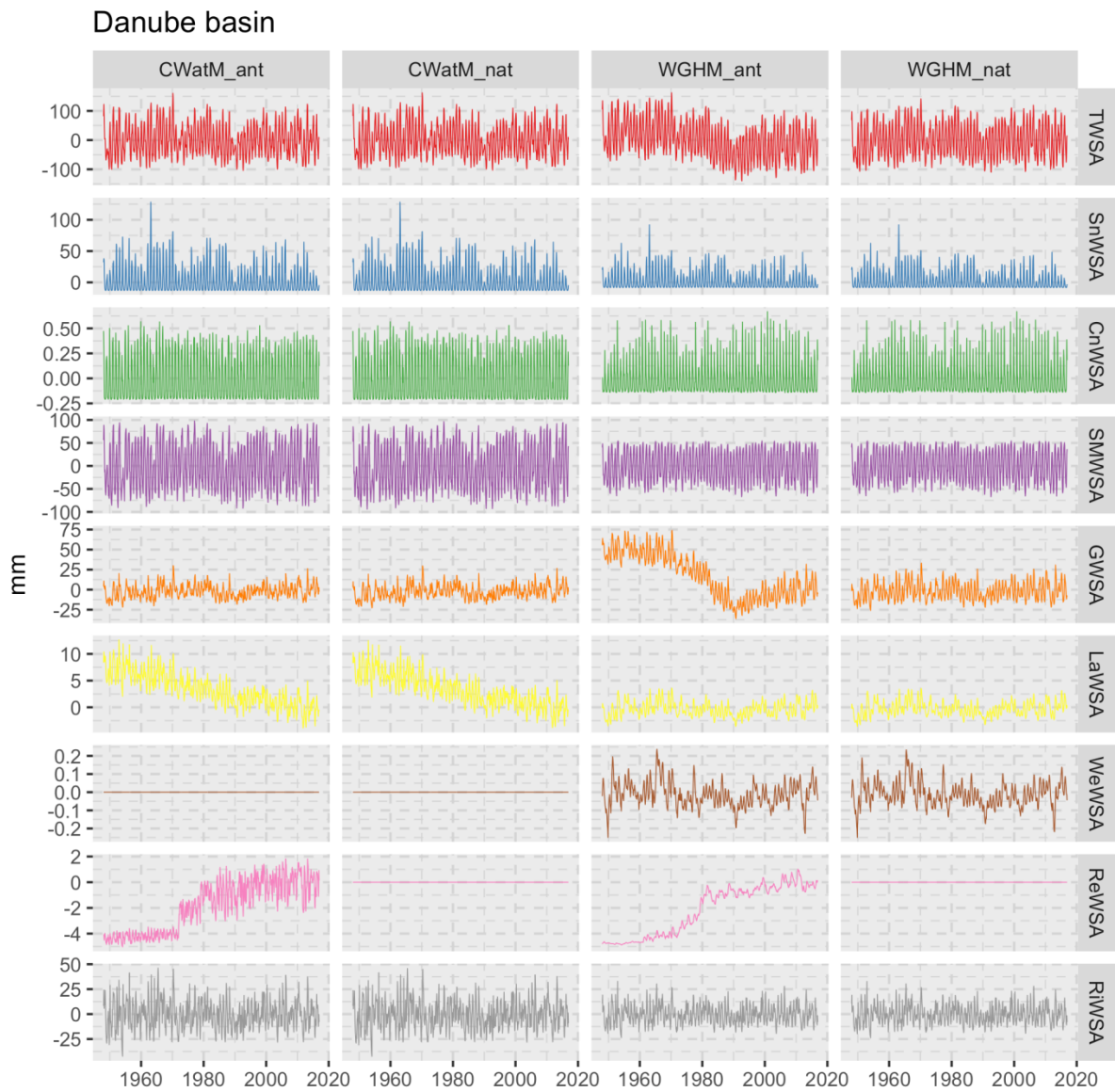
Figure C 4: As Fig. C1 but for Danube basin.
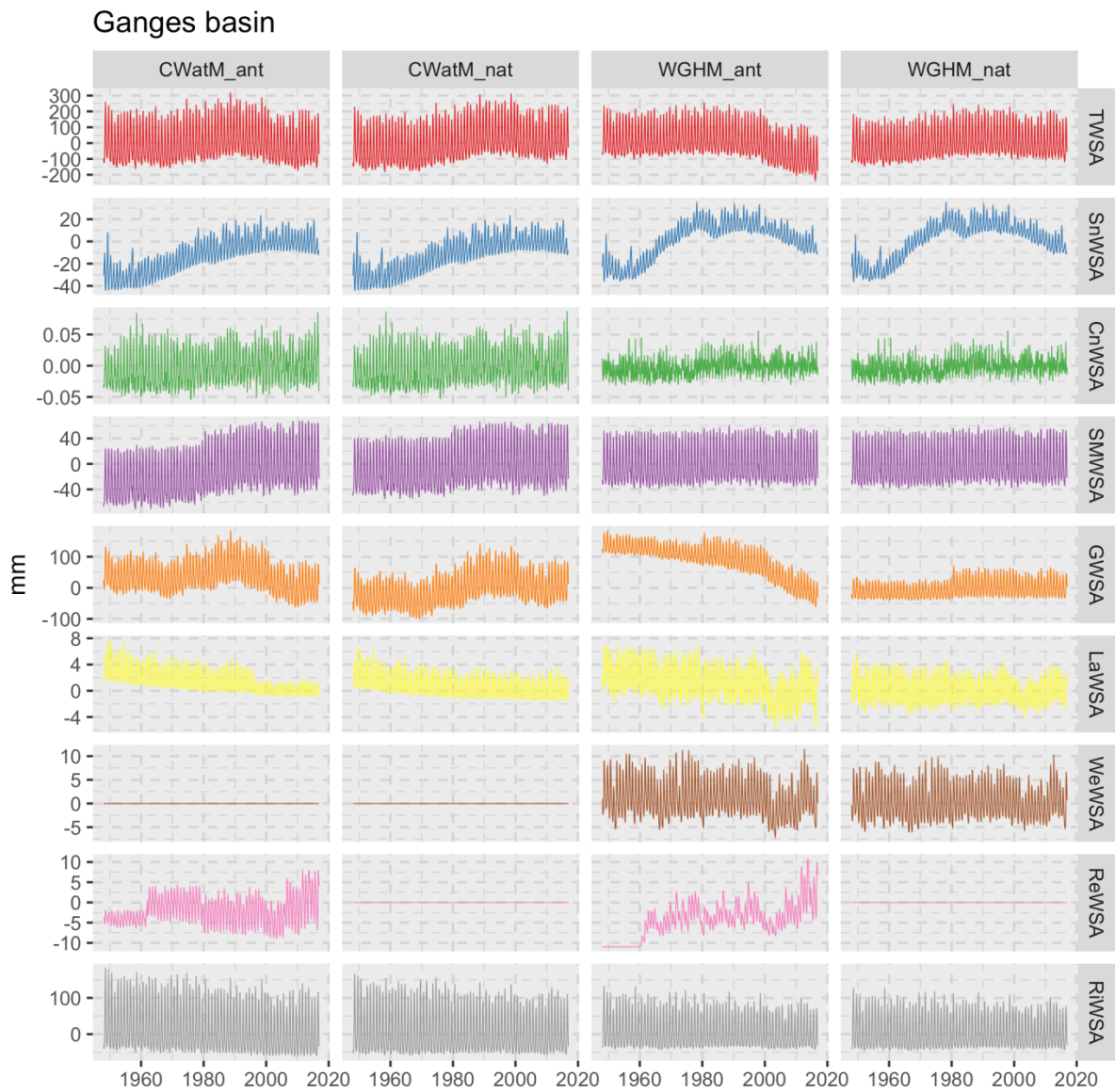
Figure C 5: As Fig. C1 but for Ganges basin.
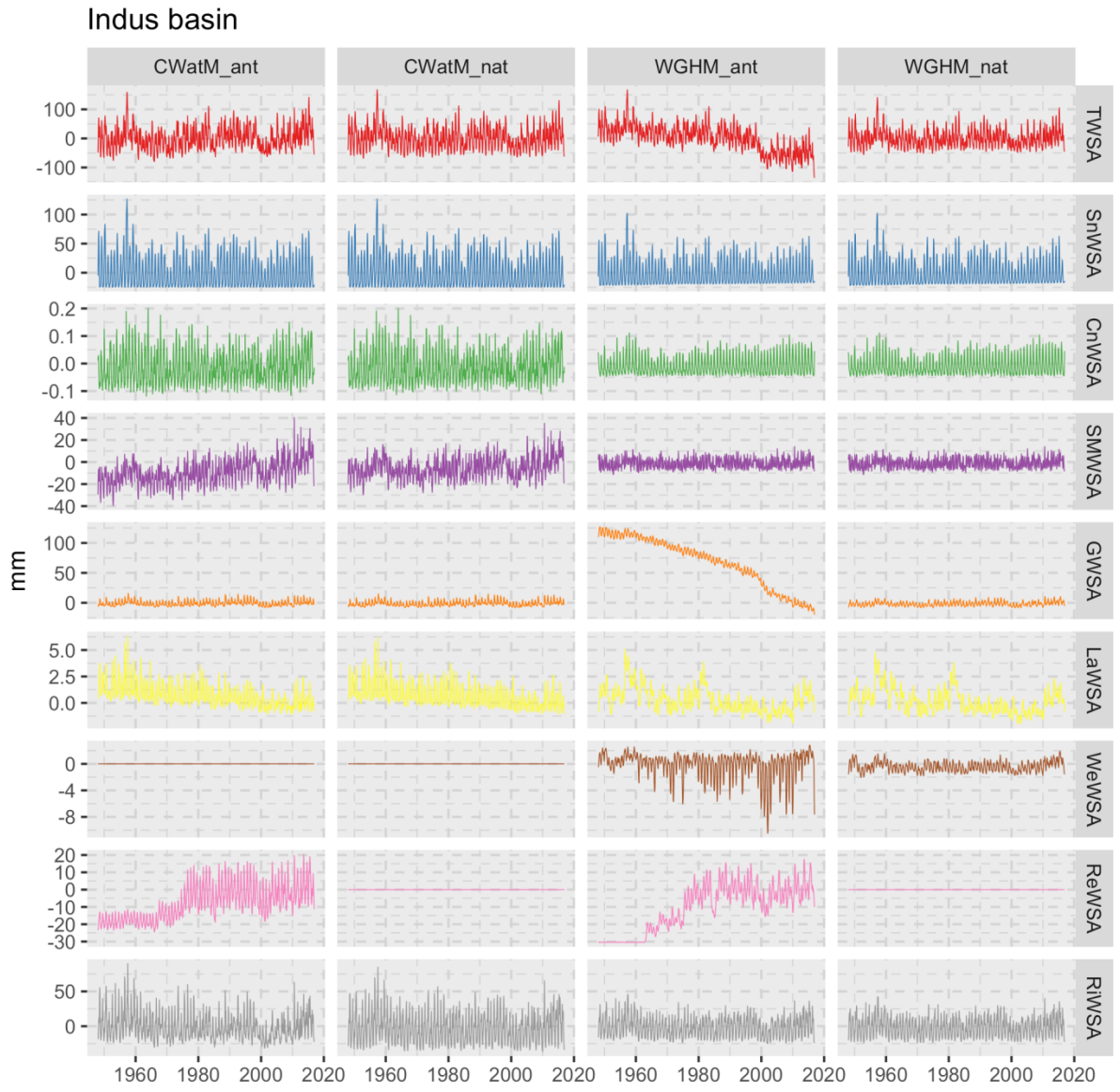
Figure C 6: As Fig. C1 but for Indus basin.
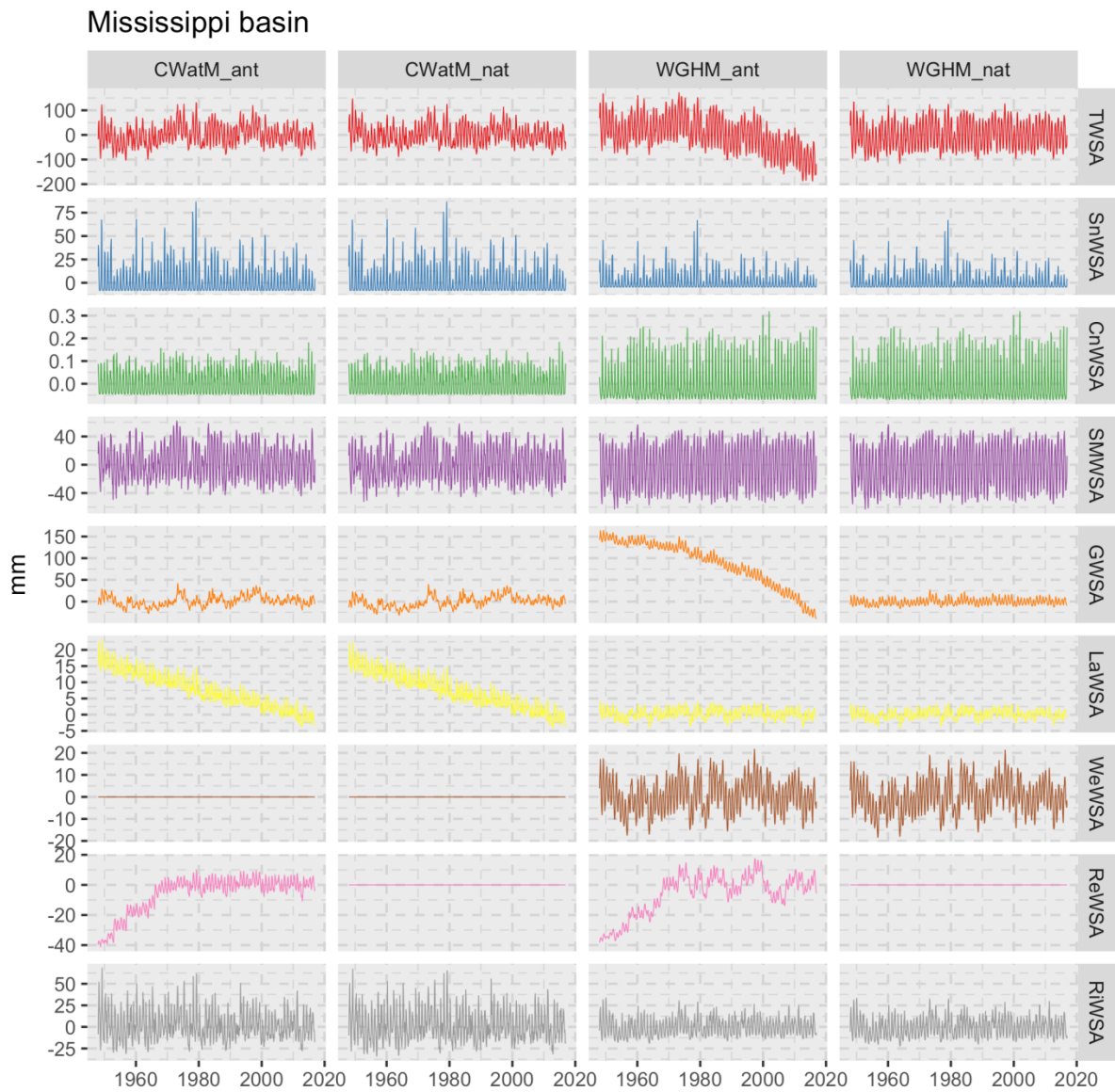
Figure C 7: As Fig. C1 but for Mississippi basin.
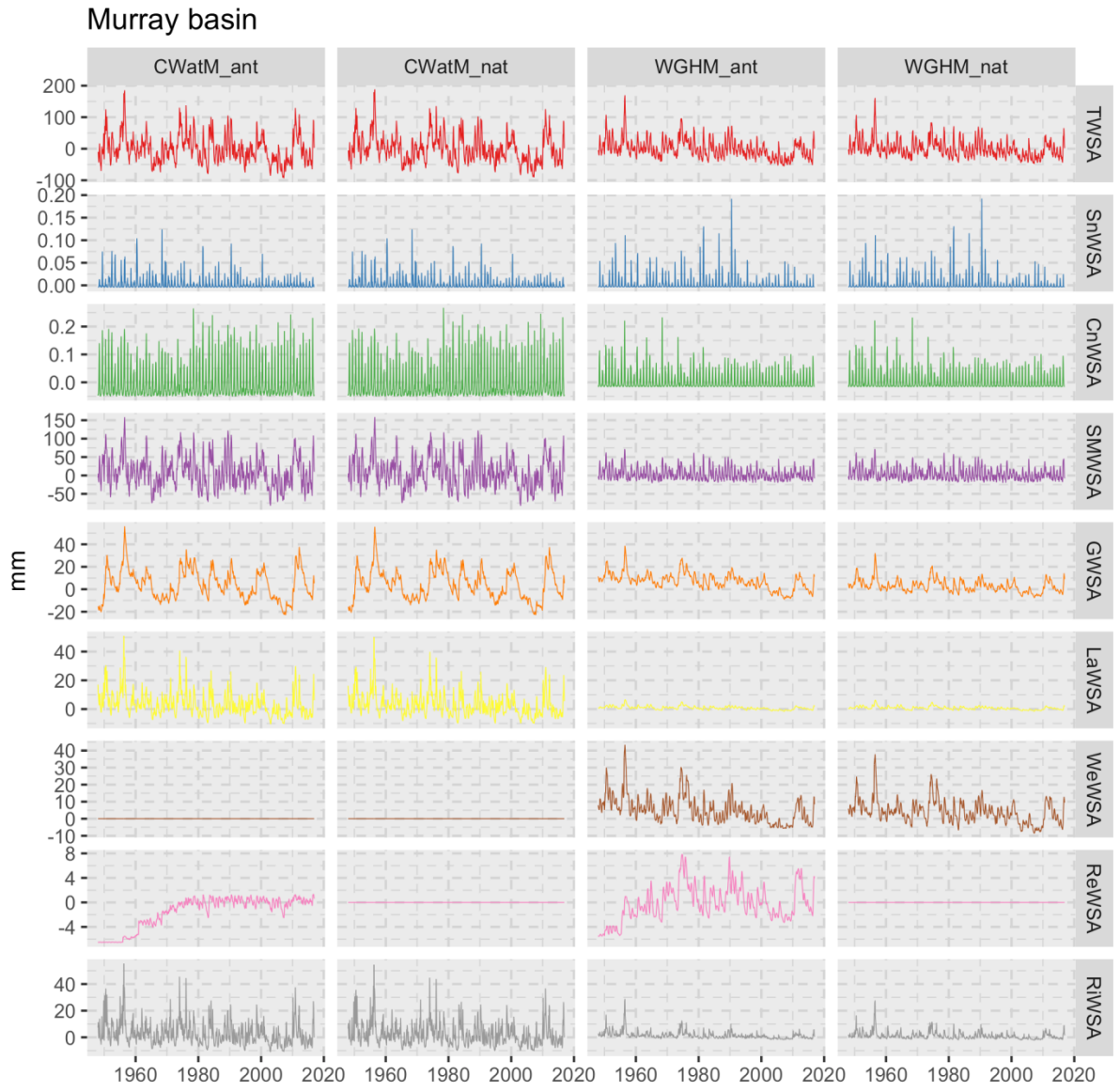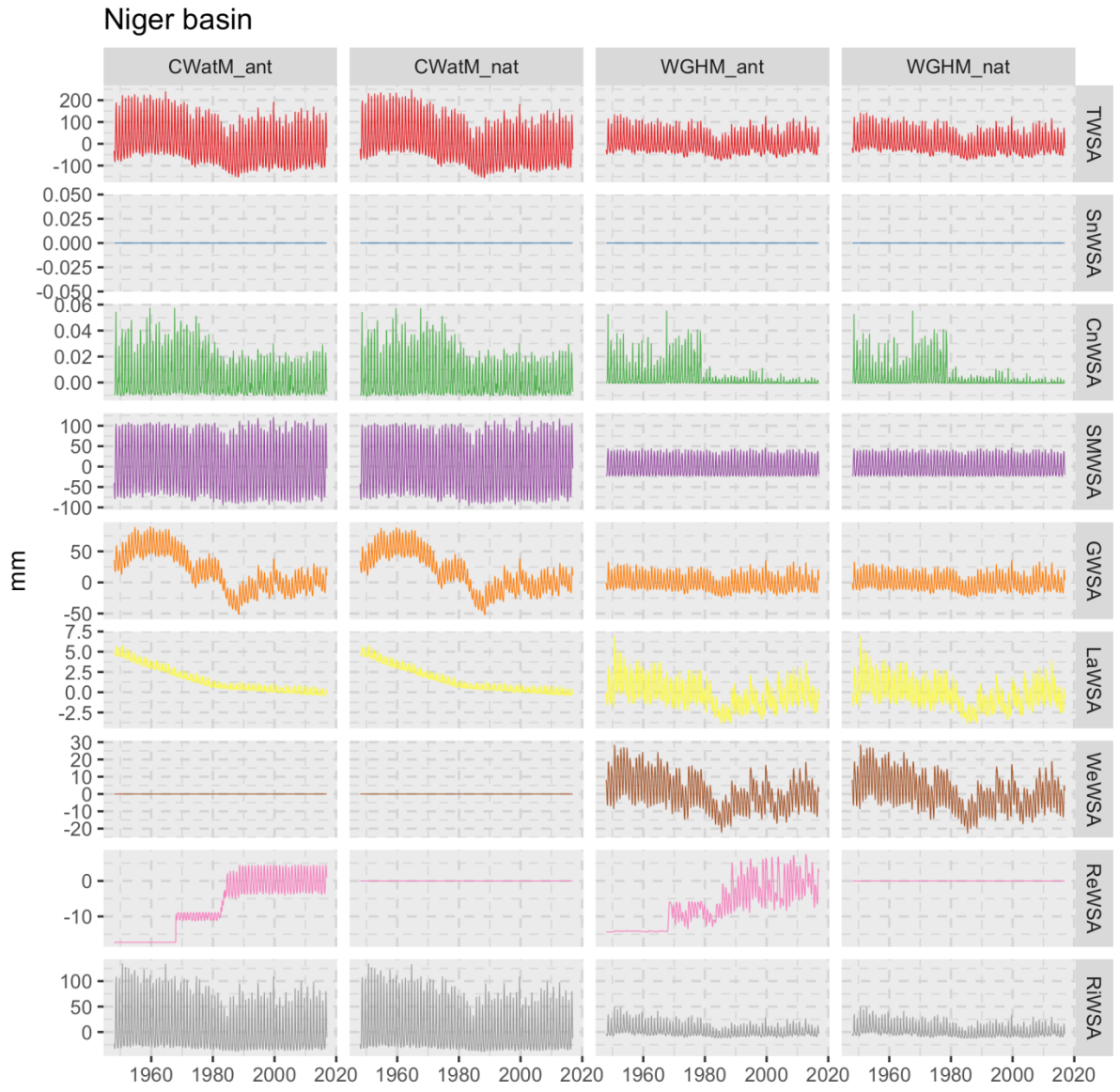
Figure C 8: As Fig. C1 but for Murray basin.

Figure C 9: As Fig. C1 but for Niger basin.

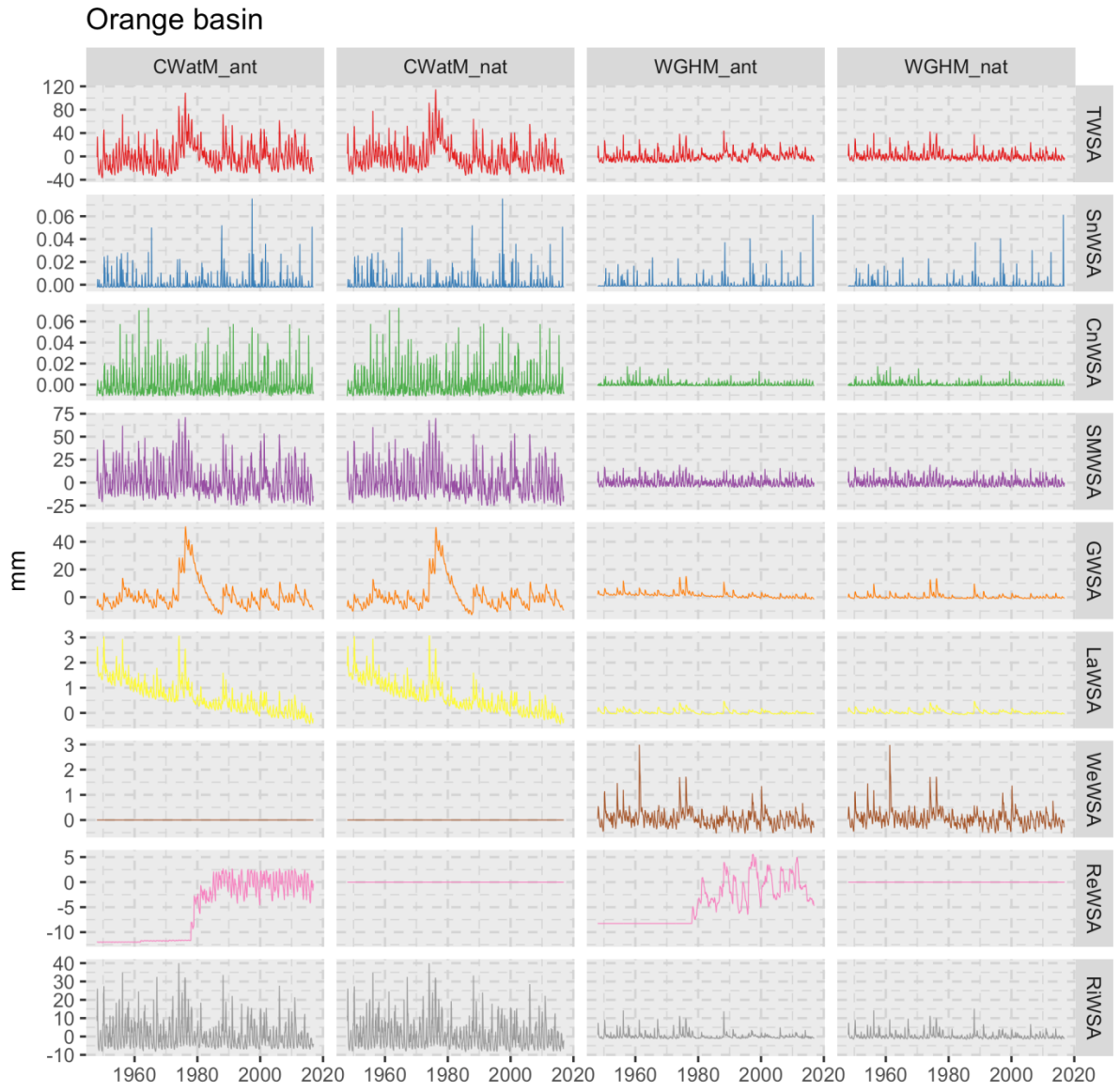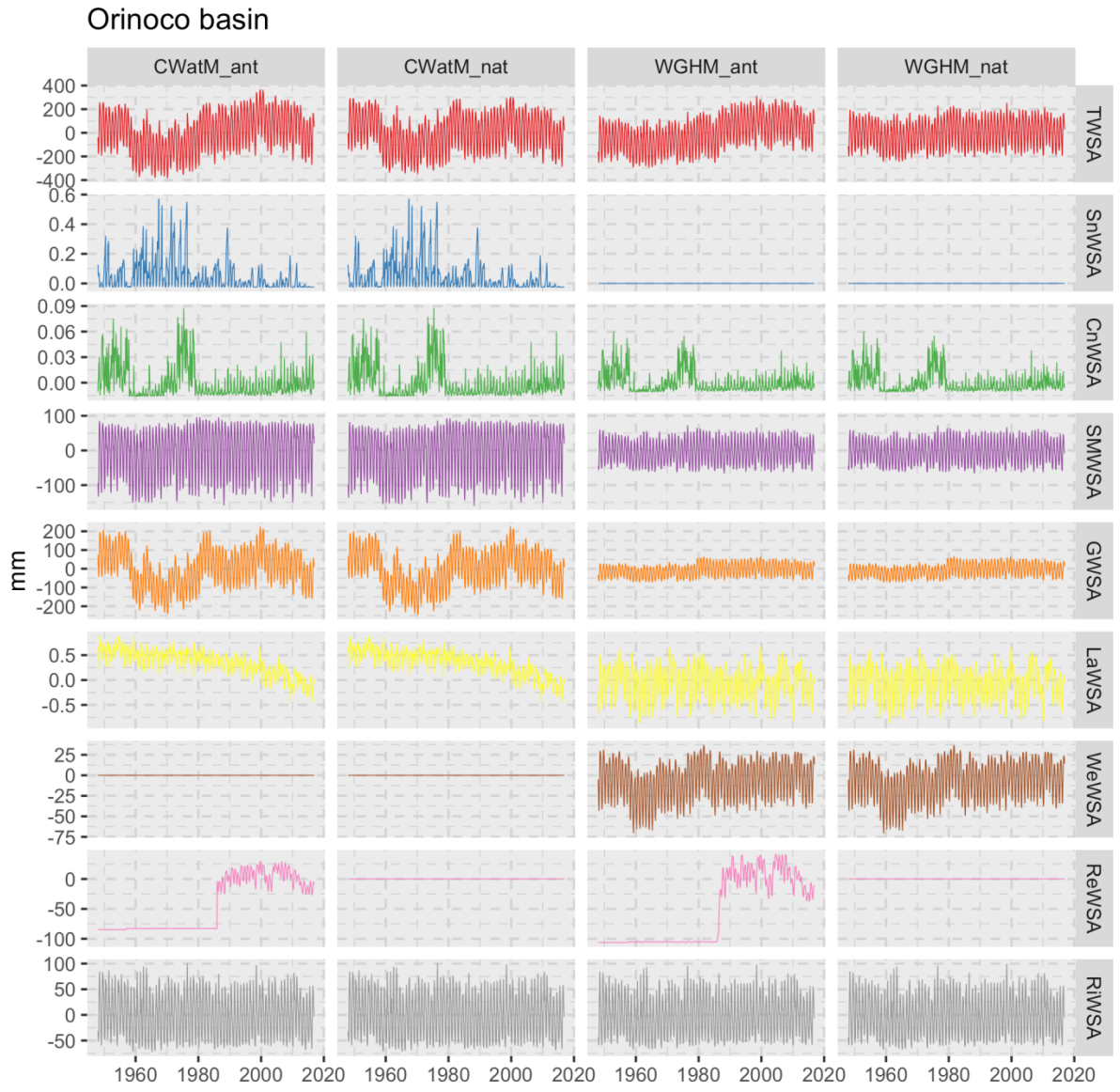Figure C 10: As Fig. C1 but for Orange basin.

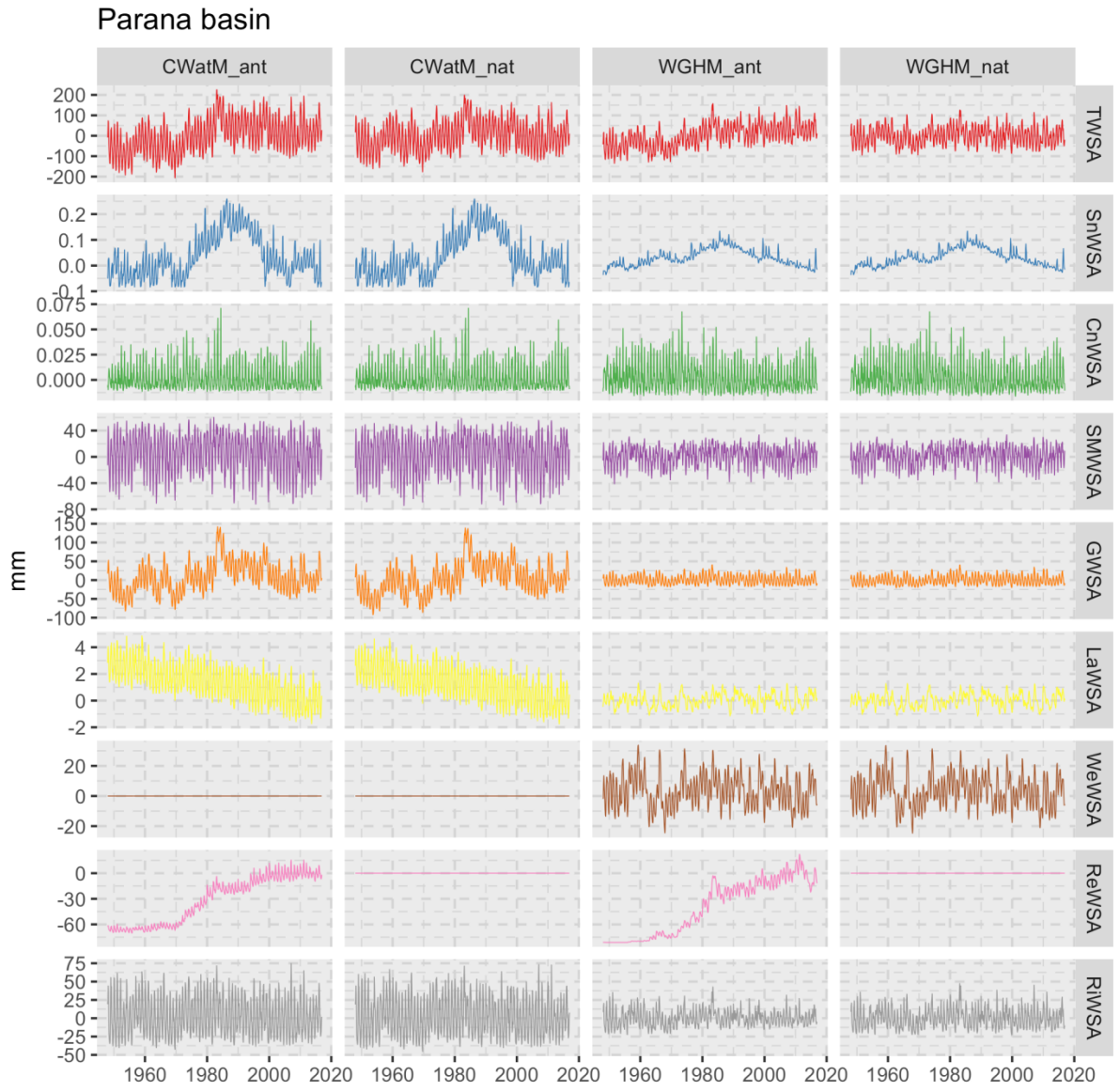*Figure C 11: As Fig. C1 but for Orinoco basin.*
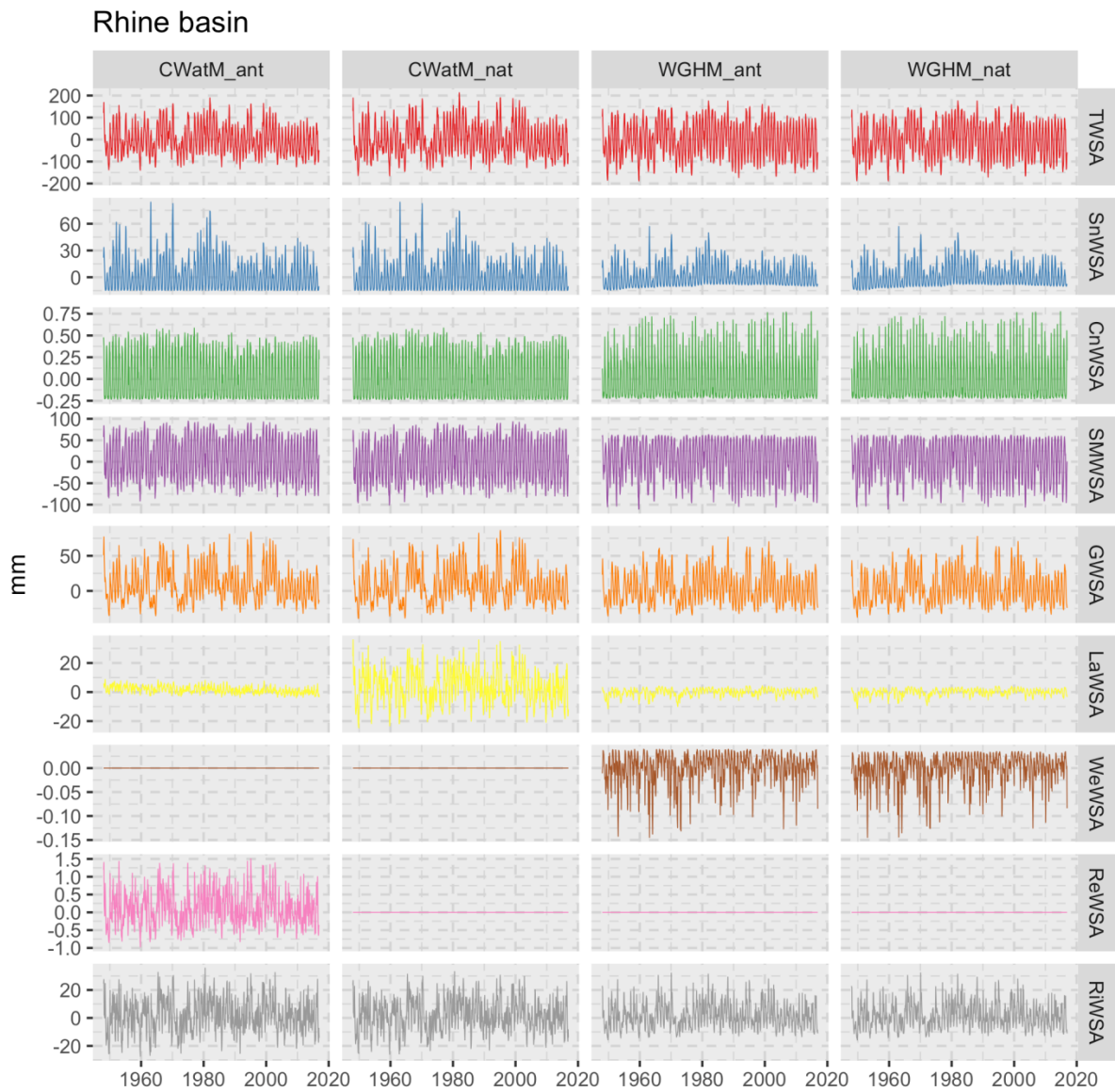
Figure C 12: As Fig. C1 but for Parana basin.

Figure C 13: As Fig. C1 but for Rhine basin.

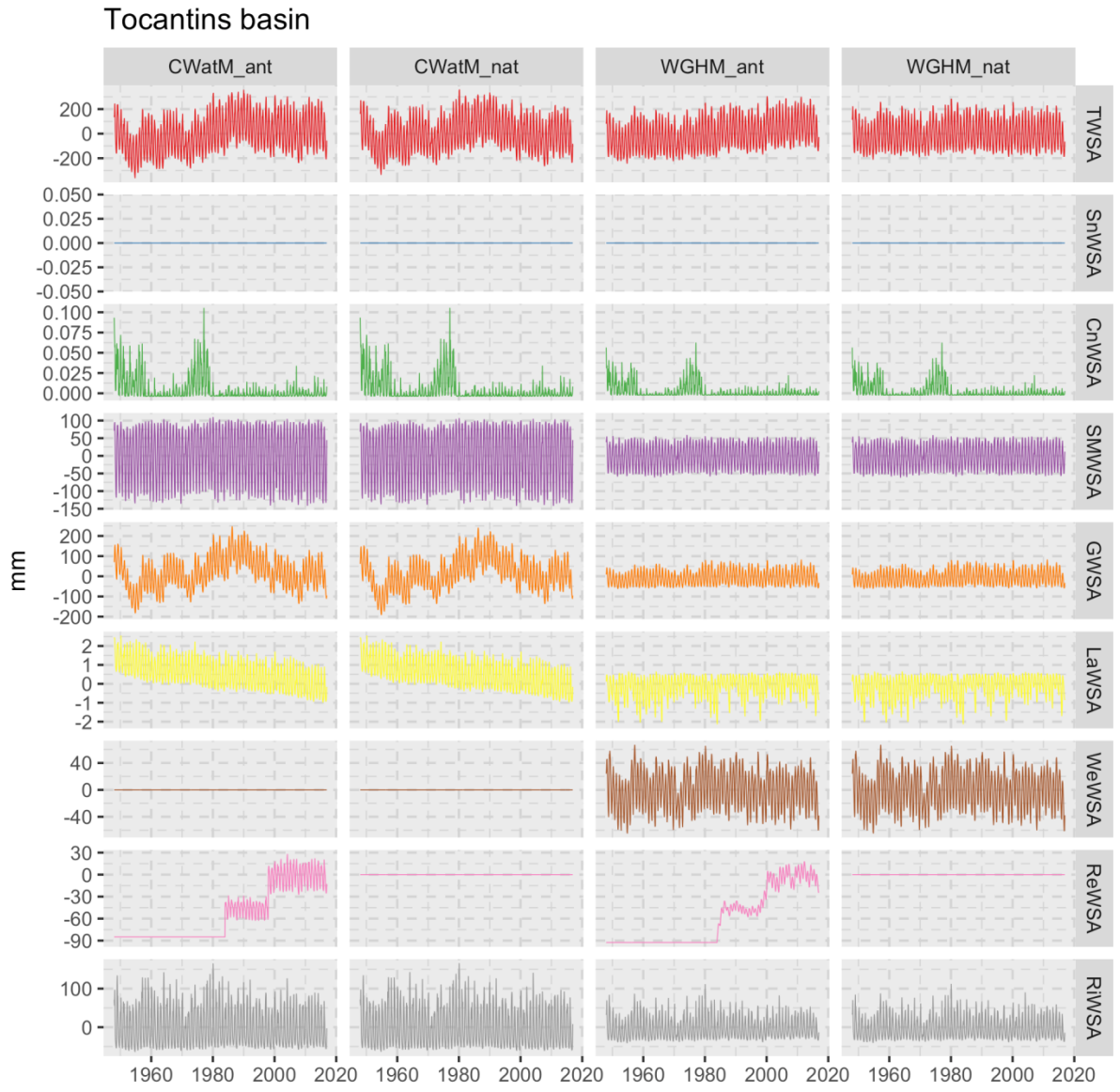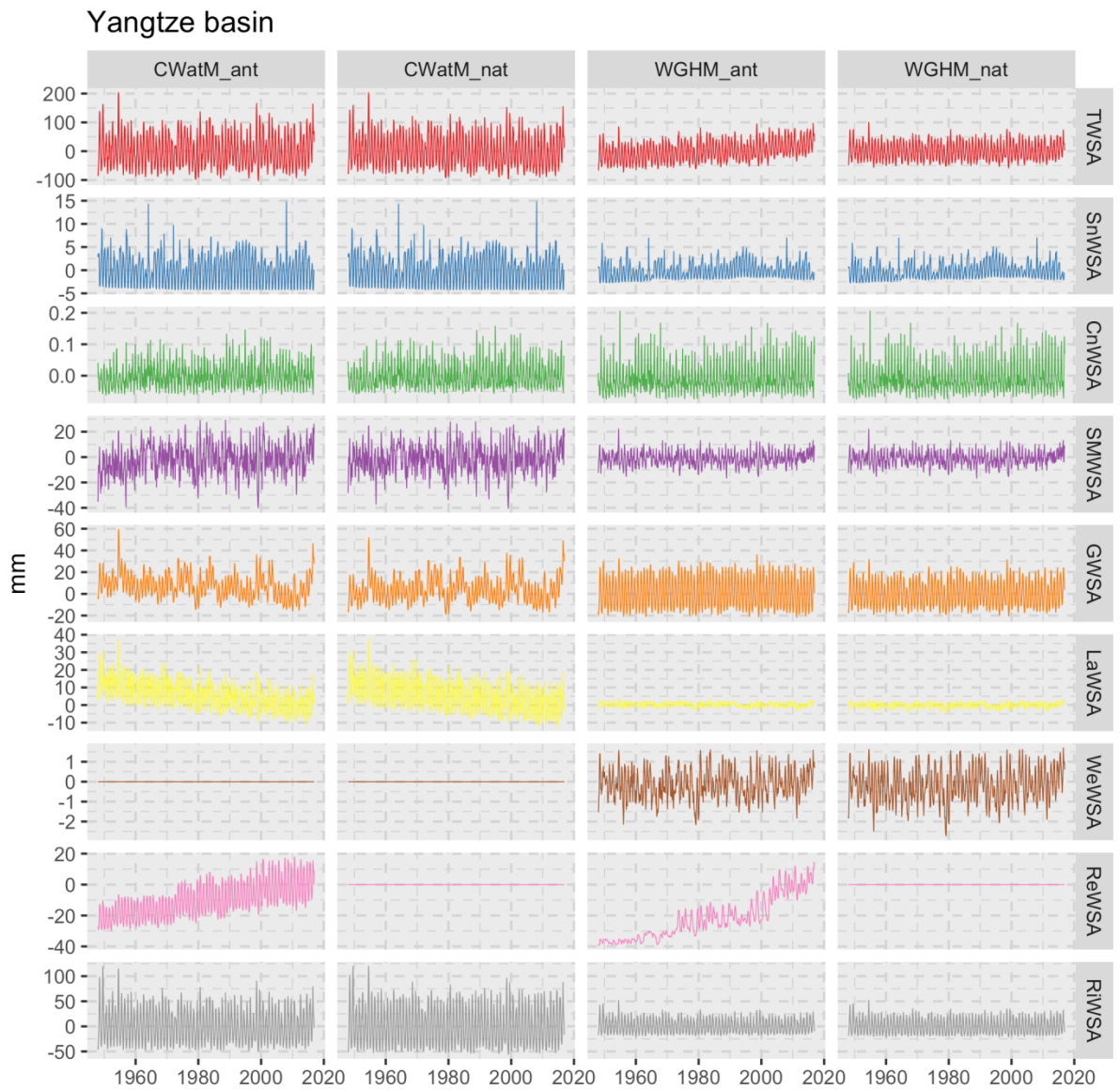*Figure C 14: As Fig. C1 but for Tocantins basin.*

Yangtze basin

Figure C 15: As Fig. C1 but for Yangtze basin.
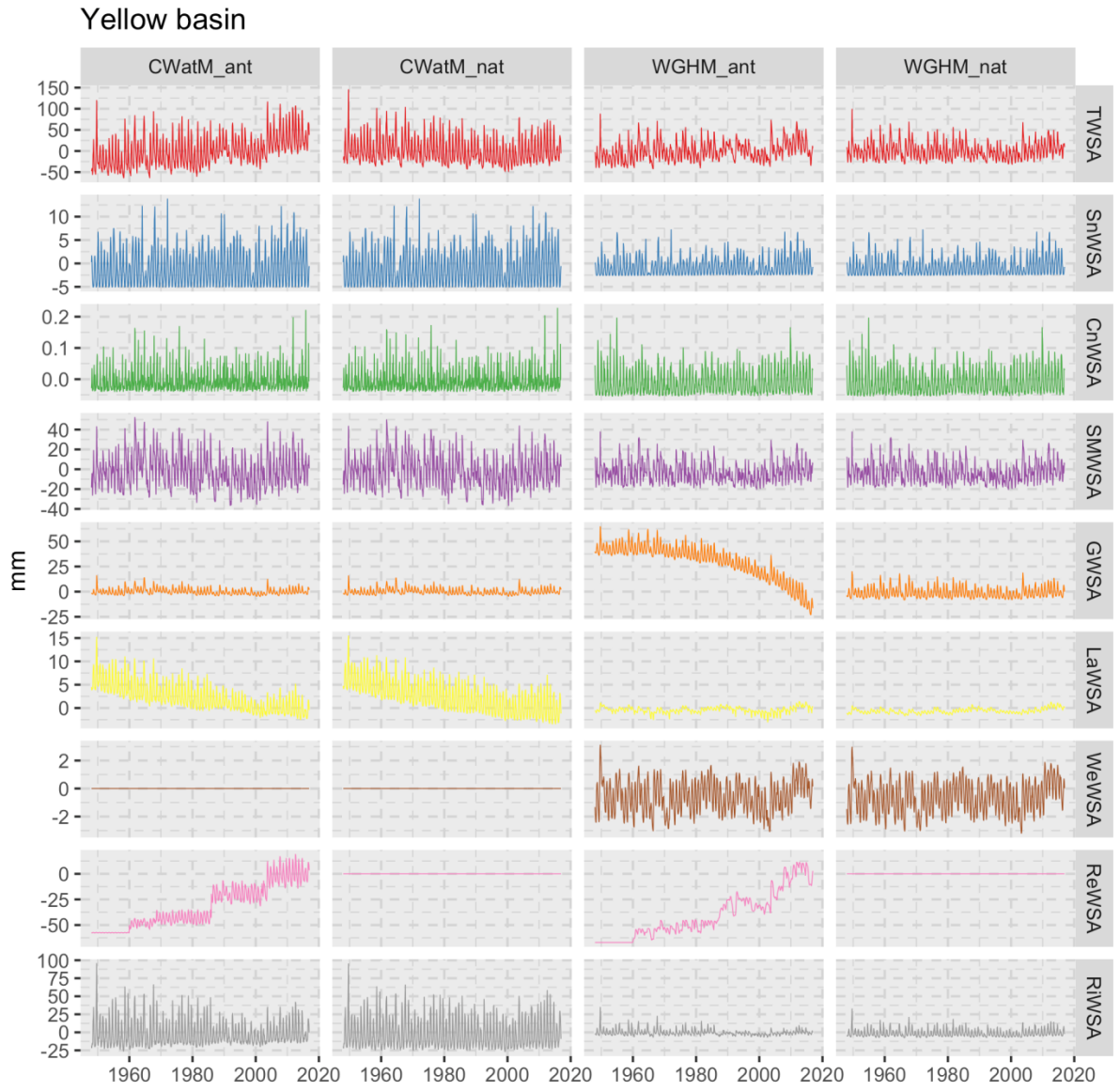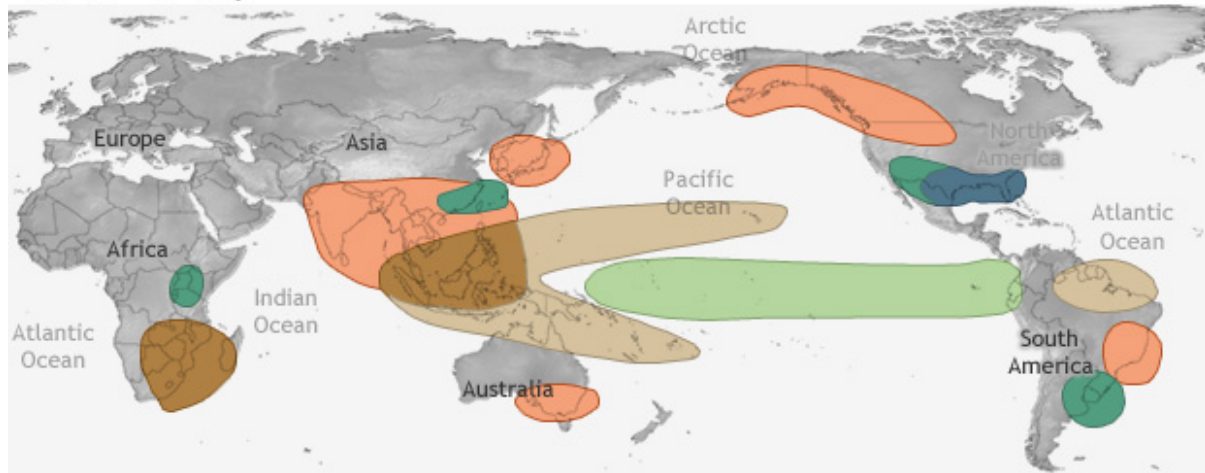
Figure C 16: As Fig. C1 but for Yellow basin.

Figure C 17: As Fig. C1 but for Zambezi basin.

Appendix D: Global impacts of El Niño and La Niña

EL NIÑO CLIMATE IMPACTS

December-February

June-August

Cool	Wet	Cool and dry	Cool and Wet
Warm	Dry	Warm and dry	Warm and wet

Figure D 1: Global maps showing the zone of influence of El Niño events and the type of climate impact during December–February (upper map) and June–August (bottom map). The maps were taken from the NOAA Climate.gov website.

LA NIÑA CLIMATE IMPACTS

December-February

Legend:
- Cool
- Warm
- Wet
- Dry
- Cool and dry
- Warm and dry
- Cool and Wet
- Warm and wet
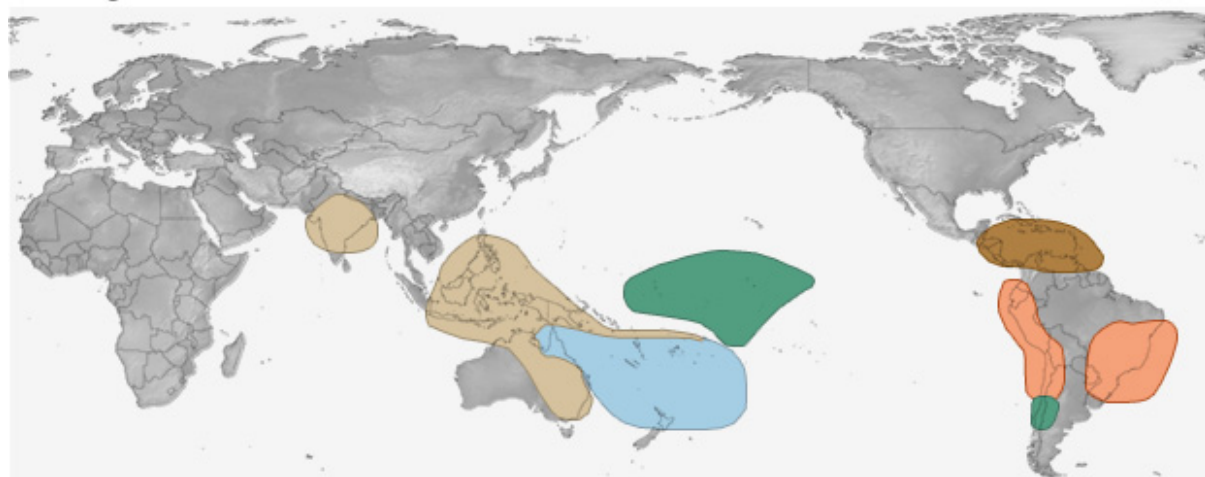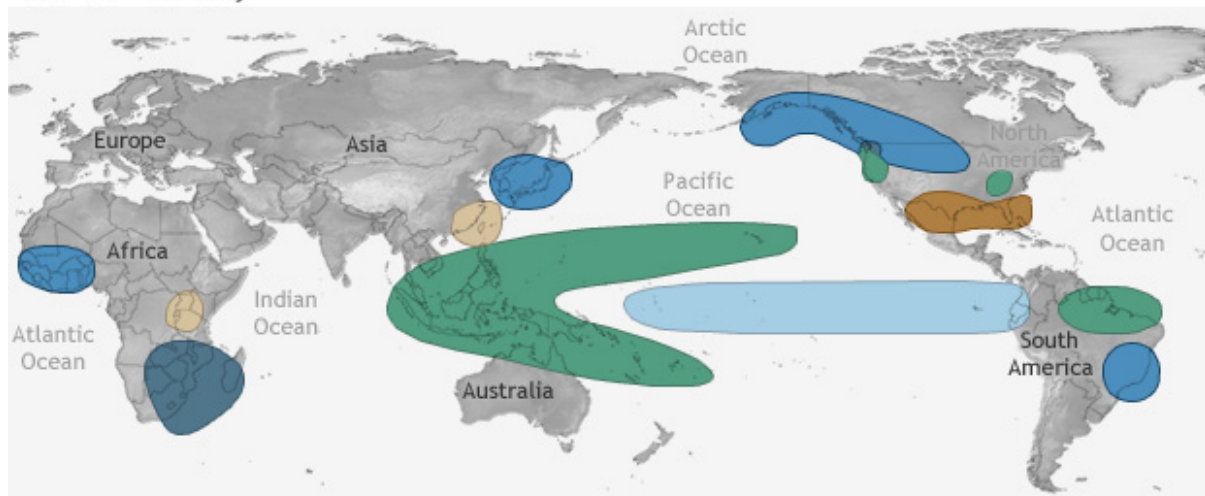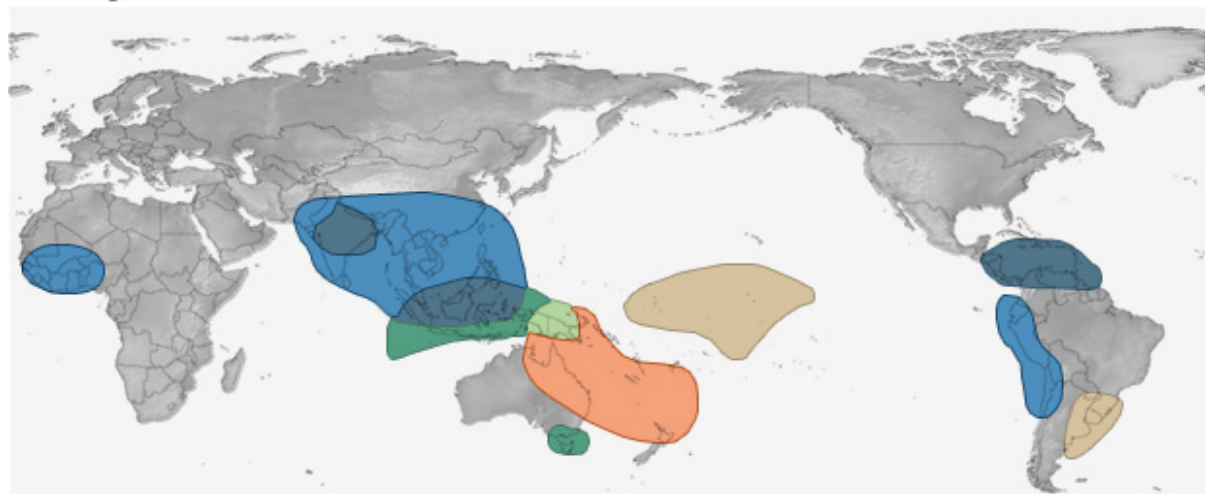
June-August

NOAA Climate.gov

Figure D 2: Global maps showing the zone of influence of La Niña events and the type of climate impact during December–February (upper map) and June–August (bottom map). The maps were taken from the NOAA Climate.gov website.

References

Boening, C., Willis, J. K., Landerer, F. W., Nerem, R. S., and Fasullo, J.: The 2011 La Niña: So strong, the oceans fell, Geophys. Res. Lett., 39, n/a-n/a, doi:10.1029/2012GL053055, 2012.

Burek, P., Satoh, Y., Kahil, T., Tang, T., Greve, P., Smilovic, M., Guillaumot, L., Zhao, F., and Wada, Y.: Development of the Community Water Model (CWatM v1.04) – a high-resolution hydrological model for global and regional assessment of integrated water resources management, Geosci. Model Dev., 13, 3267–3298, doi:10.5194/gmd-13-3267-2020, 2020.

Cáceres, D., Marzeion, B., Malles, J. H., Gutknecht, B. D., Müller Schmied, H., and Döll, P.: Assessing global water mass transfers from continents to oceans over the period 1948–2016, Hydrol. Earth Syst. Sci., 24, 4831–4851, doi:10.5194/hess-24-4831-2020, 2020.

Cazenave, A., Henry, O., Munier, S., Delcroix, T., Gordon, A. L., Meyssignac, B., Llovel, W., Palanisamy, H., and Becker, M.: Estimating ENSO Influence on the Global Mean Sea Level, 1993–2010, Marine Geodesy, 35, 82–97, doi:10.1080/01490419.2012.718209, 2012.

Cazenave, A. and Llovel, W.: Contemporary sea level rise, Annual review of marine science, 2, 145–173, doi:10.1146/annurev-marine-120308-081105, 2010.

Cazenave, A., Meyssignac, B., Ablain, M., Balmaseda, M., Bamber, J., Barletta, V., Beckley, B., Benveniste, J., Berthier, E., Blazquez, A., Boyer, T., Caceres, D., Chambers, D., Champollion, N., Chao, B., Chen, J., Cheng, L., Church, J. A., Chuter, S., Cogley, J. G., Dangendorf, S., Desbruyères, D., Döll, P., Domingues, C., Falk, U., Famiglietti, J., Fenoglio-Marc, L., Forsberg, R., Galassi, G., Gardner, A., Groh, A., Hamlington, B., Hogg, A., Horwath, M., Humphrey, V., Husson, L., Ishii, M., Jäggi, A., Jevrejeva, S., Johnson, G. C., Kolodziejczyk, N., Kusche, J., Lambeck, K., Landerer, F., Leclercq, P. W., Legresy, B., Leuliette, E., Llovel, W., Longuevergne, L., Loomis, B. D., Luthcke, S. B., Marcos, M., Marzeion, B., Merchant, C., Merrifield, M., Milne, G., Mitchum, G., Mohajerani, Y., Monier, M., Monselesan, D., Nerem, S., Palanisamy, H., Paul, F., Perez, B., Piecuch, C. G., Ponte, R. M., Purkey, S. G., Reager, J. T., Rietbroek, R., Rignot, E., Riva, R., Roemmich, D., Sørensen, L. S., Sasgen, I., Schrama, E., Seneviratne, S. I., Shum, C. K., Spada, G., Stammer, D., Velicogna, I., Schuckmann, K. von, Wada, Y., Wang, Y., Watson, C., Wiese, D., Wijffels, S., Westaway, R., Woppelmann, G., and Wouters, B.: Global sea-level budget 1993-present, doi:10.3929/ETHZ-B-000287786, 2018.

Di Long, Longuevergne, L., and Scanlon, B. R.: Uncertainty in evapotranspiration from land surface modeling, remote sensing, and GRACE satellites, Water Resour. Res., 50, 1131–1151, doi:10.1002/2013WR014581, 2014.

Dieng, H. B., Champollion, N., Cazenave, A., Wada, Y., Schrama, E., and Meyssignac, B.: Total land water storage change over 2003–2013 estimated from a global mass budget approach, Environ. Res. Lett., 10, 124010, doi:10.1088/1748-9326/10/12/124010, 2015.

Döll, P., Fiedler, K., and Zhang, J.: Global-scale analysis of river flow alterations due to water withdrawals and reservoirs, Hydrol. Earth Syst. Sci., 13, 2413–2432, doi:10.5194/hess-13-2413-2009, 2009.

Döll, P. and Lehner, B.: Validation of a new global 30-min drainage direction map, Journal of Hydrology, 258, 214–231, doi:10.1016/S0022-1694(01)00565-0, 2002.

Döll, P., Müller Schmied, H., Schuh, C., Portmann, F. T., and Eicker, A.: Global-scale assessment of groundwater depletion and related groundwater abstractions: Combining hydrological modeling with information from well observations and GRACE satellites, Water Resour. Res., 50, 5698–5720, doi:10.1002/2014WR015595, 2014.

Humphrey, V., Gudmundsson, L., and Seneviratne, S. I.: Assessing Global Water Storage Variability from GRACE: Trends, Seasonal Cycle, Subseasonal Anomalies and Extremes, Surveys in geophysics, 37, 357–395, doi:10.1007/s10712-016-9367-1, 2016.

Lehner, B. and Döll, P.: Development and validation of a global database of lakes, reservoirs and wetlands, Journal of Hydrology, 296, 1–22, doi:10.1016/j.jhydrol.2004.03.028, 2004.

Lehner, B., Liermann, C. R., Revenga, C., Vörösmarty, C., Fekete, B., Crouzet, P., Döll, P., Endejan, M., Frenken, K., Magome, J., Nilsson, C., Robertson, J. C., Rödel, R., Sindorf, N., and Wisser, D.: High-resolution mapping of the world's reservoirs and dams for sustainable river-flow management, Frontiers in Ecology and the Environment, 9, 494–502, doi:10.1890/100125, 2011.

Llovel, W., Becker, M., Cazenave, A., Jevrejeva, S., Alkama, R., Decharme, B., Douville, H., Ablain, M., and Beckley, B.: Terrestrial waters and sea level variations on interannual time scale, Global and Planetary Change, 75, 76–82, doi:10.1016/j.gloplacha.2010.10.008, 2011.

Marzeion, B., Jarosch, A. H., and Hofer, M.: Past and future sea-level change from the surface mass balance of glaciers, The Cryosphere, 6, 1295–1322, doi:10.5194/tc-6-1295-2012, 2012.

Mayer-Gürr, T., Behzadpur, S., Ellmer, M., Kvas, A., Klinger, B., Strasser, S., and Zehentner, N.: ITSG-Grace2018 - Monthly, Daily and Static Gravity Field Solutions from GRACE, 2018.

Messager, M. L., Lehner, B., Grill, G., Nedeva, I., and Schmitt, O.: Estimating the volume and age of water stored in global lakes using a geo-statistical approach, Nature communications, 7, 13603, doi:10.1038/ncomms13603, 2016.

Müller Schmied, H., Adam, L., Eisner, S., Fink, G., Flörke, M., Kim, H., Oki, T., Portmann, F. T., Reinecke, R., Riedel, C., Song, Q., Zhang, J., and Döll, P.: Variations of global and continental water balance components as impacted by climate forcing uncertainty and human water use, Hydrol. Earth Syst. Sci., 20, 2877–2898, doi:10.5194/hess-20-2877-2016, 2016.

Müller Schmied, H., Cáceres, D., Eisner, S., Flörke, M., Herbert, C., Niemann, C., Peiris, T. A., Popat, E., Portmann, F. T., Reinecke, R., Schumacher, M., Shadkam, S., Telteu, C.-E., Trautmann, T., and Döll, P.: The global water resources and use model WaterGAP v2.2d: Model description and evaluation, Geoscientific Model Development Discussions, 1–69, doi:10.5194/gmd-2020-225, 2020.

Munier, S., Palanisamy, H., Maisongrande, P., Cazenave, A., and Wood, E. F.: Global runoff anomalies over 1993–2009 estimated from coupled Land–Ocean–Atmosphere water budgets and its relation with climate variability, Hydrol. Earth Syst. Sci., 16, 3647–3658, doi:10.5194/hess-16-3647-2012, 2012.

Reager, J. T., Gardner, A. S., Famiglietti, J. S., Wiese, D. N., Eicker, A., and Lo, M.-H.: A decade of sea level rise slowed by climate-driven hydrology, Science (New York, N.Y.), 351, 699–703, doi:10.1126/science.aad8386, 2016.

Rietbroek, R., Brunnabend, S.-E., Kusche, J., Schröter, J., and Dahle, C.: Revisiting the contemporary sea-level budget on global and regional scales, Proceedings of the National Academy of Sciences of the United States of America, 113, 1504–1509, doi:10.1073/pnas.1519132113, 2016.

Rodell, M.: Basin scale estimates of evapotranspiration using GRACE and other observations, Geophys. Res. Lett., 31, doi:10.1029/2004GL020873, 2004.

Schneider, U., Becker, A., Finger, P., Meyer-Christoffer, A., Rudolf, B., and Ziese, M.: GPCC Full Data Reanalysis Version 7.0 at 0.5°: Monthly Land-Surface Precipitation from Rain-Gauges built on GTS-based and Historic Data, Research Data Archive at the National Center for Atmospheric Research, Computational and Information Systems Laboratory, Boulder, Colo. (Updated irregularly.), doi:10.5676/DWD_GPCC/FD_M_V7_050, 2015.

Tangdamrongsub, N., Han, S.-C., Tian, S., Müller Schmied, H., Sutanudjaja, E. H., Ran, J., and Feng, W.: Evaluation of Groundwater Storage Variations Estimated from GRACE Data Assimilation and State-of-the-Art Land Surface Models in Australia and the North China Plain, Remote Sensing, 10, 483, doi:10.3390/rs10030483, 2018.

Wada, Y., Reager, J. T., Chao, B. F., Wang, J., Lo, M.-H., Song, C., Li, Y., and Gardner, A. S.: Recent Changes in Land Water Storage and its Contribution to Sea Level Variations, Surveys in geophysics, 38, 131–152, doi:10.1007/s10712-016-9399-6, 2017.

Wada, Y., Wisser, D., and Bierkens, M. F. P.: Global modeling of withdrawal, allocation and consumptive use of surface water and groundwater resources, Earth Syst. Dynam., 5, 15–40, doi:10.5194/esd-5-15-2014, 2014.

Wang, J., Song, C., Reager, J. T., Yao, F., Famiglietti, J. S., Sheng, Y., MacDonald, G. M., Brun, F., Schmied, H. M., Marston, R. A., and Wada, Y.: Recent global decline in endorheic basin water storages, Nature geoscience, 11, 926–932, doi:10.1038/s41561-018-0265-7, 2018.

Weedon, G. P., Balsamo, G., Bellouin, N., Gomes, S., Best, M. J., and Viterbo, P.: The WFDEI meteorological forcing data set: WATCH Forcing Data methodology applied to ERA-Interim reanalysis data, Water Resour. Res., 50, 7505–7514, doi:10.1002/2014WR015638, 2014.

Weedon, G. P., Gomes, S., Viterbo, P., Shuttleworth, W. J., Blyth, E., Österle, H., Adam, J. C., Bellouin, N., Boucher, O., and Best, M.: Creation of the WATCH Forcing Data and Its Use to Assess Global and Regional Reference Crop Evaporation over Land during the Twentieth Century, J. Hydrometeor., 12, 823–848, doi:10.1175/2011JHM1369.1, 2011.

Wolter, K. and Timlin, M. S.: Monitoring ENSO in COADS with a seasonally adjusted principal component index, Proceedings of the 17th Climate Diagnostics Workshop, 52–57, 1993.

Wolter, K. and Timlin, M. S.: Measuring the strength of ENSO events: How does 1997/98 rank?, Weather, 53, 315–324, doi:10.1002/j.1477-8696.1998.tb06408.x, 1998.